

Exploring the Near Galactic Centre: A Comprehensive Study of Bulge OCs HSC 25, HSC 37, HSC 2878 Utilising Gaia DR3 Data

D. C. Çınar[✉]^a, W. H. Elsanhoury^{b,*}, A. A. Haroon^{c,d}

^a*Istanbul University, Institute of Graduate Studies in Science, Programme of Astronomy and Space Sciences, Beyazit, Istanbul, 34116, Turkey*

^b*Physics Department, College of Science, Northern Border University, Arar, Saudi Arabia*

^c*Astronomy and Space Science Department, Faculty of Science, King Abdulaziz University, Jeddah, Saudi Arabia*

^d*Astronomy Department, National Research Institute of Astronomy and Geophysics (NRIAG), Helwan, 11421, Cairo, Egypt*

Abstract

We present a comprehensive photometric and kinematic study of the open clusters HSC 25, HSC 37, and HSC 2878, located in the innermost regions of the Galactic disc. Utilizing data from *Gaia* DR3 and the UPMASK membership algorithm, we identify 44, 55, and 112 most probable members for HSC 25, HSC 37, and HSC 2878, respectively. The mean proper-motion components are obtained as $(-5.901 \pm 0.41, -6.213 \pm 0.40)$, $(-3.231 \pm 0.56, -4.564 \pm 0.47)$, and $(-3.830 \pm 0.51, -5.198 \pm 0.44)$ mas yr $^{-1}$ for HSC 25, HSC 37, and HSC 2878, respectively. The open clusters span a broad range of evolutionary stages, with estimated ages of $\log(t/\text{yr}) = 8.38 \pm 0.08$, 7.04 ± 0.09 , and 9.04 ± 0.09 , and corresponding heliocentric distances of 7.36 ± 0.37 , 6.79 ± 0.18 , and 6.17 ± 0.22 kpc. The obtained metallicities are 0.0388 ± 0.0039 , 0.0259 ± 0.0028 , and 0.0209 ± 0.0023 , respectively. Total mass estimates are 135 , 755 , and $204 M_{\odot}$, respectively, highlighting notable differences in stellar content across the clusters. An analysis of dynamical relaxation times suggests that HSC 25 and HSC 2878 are dynamically evolved, whereas the much younger HSC 37 is still in an early phase of dynamical evolution. The high space velocities and orbital parameters of these clusters reveal significant deviations from typical disc kinematics. HSC 25 and HSC 37 exhibit eccentric orbits and small perigalactic distances, consistent with dynamically heated or accreted origins within the Galactic bulge. In contrast, HSC 2878's relaxed, planar orbit suggests in situ bulge membership despite its age. These findings point toward a heterogeneous dynamical origin for the clusters, with implications for star formation and evolution in the inner Milky Way.

Keywords: Galaxy: open clusters and associations; individual: HSC 25, HSC 37, HSC 2878, Stellar kinematics, Cluster dynamics, HR diagram

1. Introduction

Open clusters (OCs) are gravitationally bound stellar groups that emerge from the collapse of giant molecular clouds, representing fundamental building blocks of star formation in the Milky Way (MW) (Lada & Lada, 2003; Kroupa, 2001). Sharing a common origin, member stars exhibit similar chemical compositions, distances, and formation timescales, rendering OCs critical for tracing Galactic stellar populations and structure. While OCs are found across the Galactic disc, their presence in the inner regions, closer to the Galactic centre, is of particular interest due to the complex dynamical environment and the role these OCs play in probing the evolution of the central Galaxy.

The stellar populations within OCs span a broad mass range, resulting in significant diversity in luminosities, effective temperatures, and spectral types (Bastian et al.,

2010). Over time, internal dynamical effects such as mass segregation, coupled with external perturbations including tidal stripping induced by the Galactic gravitational field, reshape the structure and membership of OCs (Binney & Tremaine, 2008). Besides mapping the Galaxy's formation history, OCs, especially those located near the Galactic centre, serve as essential calibrators for stellar evolutionary models across various age ranges, from young embedded OCs to older, dynamically evolved systems like M67 or NGC 188 (Perryman et al., 1998; Çınar et al., 2024). These characteristics firmly establish OCs as vital laboratories for studying both stellar and Galactic evolution.

The region near the Galactic centre has been investigated in the literature using a variety of Galactocentric distance thresholds (Bobylev & Bajkova, 2017; Carvajal, 2022; Braga et al., 2019; Zoccali & Valenti, 2024; Sales-Silva et al., 2024; Nepal et al., 2025). In this study, we adopt a more conservative limit of 2 kpc to define the inner Galaxy. This region is known to be dynamically complex and is dominated by the influence of the central Galactic bar. Observational evidence—beginning with HI

*Corresponding author: W. H. Elsanhoury

Email addresses: denizcennetçınar@gmail.com (D. C. Çınar[✉]), elsanhoury@nbu.edu.sa (W. H. Elsanhoury[✉])

studies from the Green Bank telescope in 1978 (Liszt & Burton, 1980) and followed by dynamical models and confirmations (Binney et al., 1991)—has demonstrated that the gas and stellar kinematics within this radius are significantly shaped by a bar-like potential. Near-infrared observations Blitz & Spergel, 1991; Dwek et al., 1995, e.g. further revealed a triaxial bulge with a marked left–right asymmetry in flux distribution, emphasising the morphological and dynamical distinctiveness of this region compared to the outer disc. The OCs selected for investigation in this study, HSC 25, HSC 37, and HSC 2878, are among the nearest ($R_{\text{GC}} < 2$ kpc) known OCs to the Galactic centre (Zoccali & Valenti, 2024). Despite their intriguing locations within the inner Galaxy, these OCs have remained largely unexamined in the literature, with no detailed analyses reported thus far. Their existence has been documented only in the Hunt & Reffert (2024) catalogue, which provides limited information. This lack of comprehensive study underscores a significant gap in our knowledge of stellar populations and dynamical conditions in the central regions of the MW.

The dense distribution of interstellar dust toward the Galactic centre causes intense and irregular extinction, posing a major challenge for the accurate photometric analysis of clusters in these regions. This leads to significant reddening effects, which can alter the observed photometric properties of stars and complicate the determination of fundamental cluster parameters such as distance, age, and metallicity (Banks et al., 2020). In particular, differential reddening across the field can distort colour–magnitude diagrams (CMDs) and introduce systematic uncertainties in isochrone fitting (Bilir et al., 2010, 2016). Accurate modelling of these extinction effects is therefore essential to reliably characterise clusters projected onto the inner Galactic regions.

The fundamental parameters of HSC 25, HSC 37, and HSC 2878, as reported in the Hunt & Reffert (2024) catalogue, are summarised below. HSC 25 is located at $\alpha_{\text{ICRS}} = 265^\circ.392$ and $\delta_{\text{ICRS}} = -25^\circ.702$, with proper-motion components ($\mu_\alpha \cos \delta, \mu_\delta$) of $(-5.898, -6.197)$ mas yr^{-1} , and a trigonometric parallax of 0.053 mas. Its estimated distance is approximately 9.89 kpc, with a mean logarithmic age of $\log t = 8.903$. The cluster exhibits a mean colour excess of $E(G_{\text{BP}} - G_{\text{RP}}) = 2.568$ mag and a V -band extinction of $A_V = 5.718$ mag.

HSC 37 is positioned at $\alpha_{\text{ICRS}} = 264^\circ.355$ and $\delta_{\text{ICRS}} = -24^\circ.406$, with proper-motion components ($\mu_\alpha \cos \delta, \mu_\delta$) of $(-3.173, -4.548)$ mas yr^{-1} , and a trigonometric parallax of 0.097 mas. The cluster is located at a distance of approximately 6.75 kpc and has a mean logarithmic age of $\log t = 7.260$. Its mean colour excess and V -band extinction are measured as $E(G_{\text{BP}} - G_{\text{RP}}) = 1.944$ mag and $A_V = 4.329$ mag, respectively.

HSC 2878 is found at $\alpha_{\text{ICRS}} = 256^\circ.102$ and $\delta_{\text{ICRS}} = -37^\circ.011$, with proper-motion components ($\mu_\alpha \cos \delta, \mu_\delta$) of $(-3.837, -5.103)$ mas yr^{-1} , and a trigonometric paral-

lax of 0.094 mas. Its estimated distance is approximately 7.22 kpc, and the mean logarithmic age is determined as $\log(t/\text{yr}) = 9.052$. The colour excess and V -band extinction values for this OC are $E(G_{\text{BP}} - G_{\text{RP}}) = 2.186$ mag and $A_V = 4.868$ mag, respectively.

The structure of this paper is organised as follows: Section 2 introduces with *Gaia* DR3 as main data sources. Section 3 describes the analysis and results of astrometric and photometric datasets, luminosity and mass functions, dynamical, velocity ellipsoid parameters, and the orbital parameters for the analysis of the OCs HSC 25, HSC 37, and HSC 2878. Section 4 summarises the main results and highlights their implications for the understanding of stellar systems in the inner Galaxy.

2. Gaia DR3 Data

The present analysis relies predominantly on the third data release of the *Gaia* mission, known as *Gaia* DR3 (Gaia Collaboration et al., 2023), as the principal resource for studying the stellar populations of three OCs: HSC 25, HSC 37, and HSC 2878. Publicly released on 13 June 2022, *Gaia* DR3 incorporates a significant expansion in both astrometric and photometric data content compared to previous releases. It provides precise multi-band photometry in the G , G_{BP} , and G_{RP} passbands, along with radial velocity measurements for over 33 million stars. In particular, its parallax measurements reach uncertainties as low as 0.02 to 0.03 mas for stars with $G < 15$ mag, increasing to approximately 1.3 mas at $G = 21$ mag. Proper motion uncertainties follow a similar pattern, ranging from 0.02–0.03 mas yr^{-1} for brighter sources to about 1.4 mas yr^{-1} for the faintest objects.

For each of the three OCs, a circular region of 20 arcminutes radius around the nominal cluster centre was used to extract data from *Gaia* DR3. This dataset includes three-band photometric values ($G, G_{\text{BP}}, G_{\text{RP}}$), astrometric positions (right ascension α and declination δ), proper-motion components ($\mu_\alpha \cos \delta, \mu_\delta$), and trigonometric parallaxes (ϖ), each accompanied by their associated errors. All astrometric and photometric parameters, along with their associated uncertainties, were taken into account during the analysis. Based on the central coordinates, a total of 331,121 stellar sources were retrieved from the *Gaia* DR3 database within a radius of 20 arcminutes centred on HSC 25, 325,111 stars around HSC 37, and 202,316 stars around HSC 2878. Table 1 presents the mean internal photometric uncertainties ($\sigma_G, \sigma_{(G_{\text{BP}} - G_{\text{RP}})}$) and astrometric uncertainties, including proper-motion component errors ($\sigma_{\mu_{\alpha*}}, \sigma_{\mu_\delta}$), total proper motion errors (σ_μ), and trigonometric parallax errors (σ_ϖ), based on *Gaia* DR3 data, calculated for all retrieved sources within the field of view of HSC 25, HSC 37, and HSC 2878, in different G -band magnitude bins.

This study focuses on the OCs HSC 25, HSC 37, and HSC 2878, which were identified from the catalogue of candidate stellar associations recently compiled by (Hunt

Table 1: Mean internal photometric uncertainties (σ_G , $\sigma_{G_{\text{BP}}-G_{\text{RP}}}$) and astrometric uncertainties (σ_μ , σ_ϖ) as a function of G -band magnitude for HSC 25, HSC 37, and HSC 2878. These statistics, as well as the reported star counts, are computed for all sources within the analyzed field of view, prior to any membership selection.

G (mag)	N	σ_G (mag)	$\sigma_{G_{\text{BP}}-G_{\text{RP}}}$ (mag)	σ_μ (mas yr $^{-1}$)	σ_ϖ (mas)
HSC 25					
(06,14]	302	0.003	0.007	0.048	0.040
(14,15]	733	0.004	0.015	0.061	0.051
(15,16]	3266	0.004	0.021	0.089	0.074
(16,17]	8636	0.003	0.023	0.115	0.096
(17,18]	23,275	0.003	0.038	0.192	0.161
(18,19]	57,690	0.004	0.077	0.322	0.265
(19,20]	70,717	0.005	0.162	0.762	0.638
(20,21]	152,106	0.008	0.284	1.589	1.267
(21,22]	14,396	0.022	0.313	3.351	2.527
HSC 37					
(06,14]	271	0.003	0.009	0.044	0.036
(14,15]	872	0.003	0.013	0.061	0.050
(15,16]	3062	0.003	0.014	0.078	0.064
(16,17]	7353	0.003	0.016	0.110	0.091
(17,18]	23,103	0.003	0.030	0.183	0.151
(18,19]	33,146	0.004	0.064	0.335	0.270
(19,20]	64,345	0.005	0.140	0.920	0.762
(20,21]	180,897	0.009	0.251	1.808	1.350
(21,22]	12,062	0.032	0.182	3.034	2.052
HSC 2878					
(06,14]	552	0.003	0.008	0.043	0.030
(14,15]	960	0.003	0.009	0.052	0.036
(15,16]	2571	0.003	0.010	0.073	0.050
(16,17]	5356	0.003	0.013	0.111	0.076
(17,18]	1,2179	0.003	0.024	0.193	0.130
(18,19]	23,967	0.004	0.051	0.334	0.228
(19,20]	45,349	0.005	0.112	0.686	0.480
(20,21]	100,566	0.008	0.211	1.716	0.973
(21,22]	10,816	0.025	0.195	3.136	2.016

& Reffert, 2024). This comprehensive catalogue provides updated positions, structural parameters, and preliminary classifications for a large sample of OCs, incorporating both astrometric and photometric data primarily drawn from the *Gaia* DR3 archive. While many of the entries in the Hunt & Reffert (2024) catalogue have been explored in earlier studies targeting their photometric characteristics or dynamical states (e.g., Elsanhoury et al., 2025; Haroon et al., 2025a; Alzhrani et al., 2025; Yousef Alzahrani et al., 2025b), these three particular OCs have remained largely uncharacterised in the literature. In the present work, we conduct a detailed membership analysis and structural examination of HSC 25, HSC 37, and HSC 2878 using the high-precision data from *Gaia* DR3.

3. Analysis and Results

In this study, we employed the Unsupervised Photometric Membership Assignment in Stellar Clusters (UPMASK) algorithm (Krone-Martins & Moitinho, 2014) to determine the membership probabilities ($P \geq 50\%$) of stars associated with the targeted OCs. UPMASK is a robust and widely-utilised tool in cluster studies, designed to identify

coherent stellar populations by combining astrometric and photometric information in a statistically principled manner.

The method operates through a k -means clustering approach, grouping stars based on their similarity in astrometric parameters, namely proper-motion components ($\mu_\alpha \cos \delta$, μ_δ) and trigonometric parallaxes (ϖ), while assessing the significance of these groupings through randomisation tests. For this analysis, we utilised precise astrometric measurements from the *Gaia* DR3 catalogue, incorporating right ascension (α), declination (δ), proper-motion components, trigonometric parallaxes, and their associated uncertainties into the algorithm.

Following the recommendations of Krone-Martins & Moitinho (2014) for poorly populated stellar systems, and considering the intrinsically sparse nature of our targets, particularly HSC 25 and HSC 37, we adopted relatively small values for the number of stars per k -means cluster (n), tailored to each system. Specifically, we set $n = 7$ for HSC 25, $n = 10$ for HSC 37, and $n = 15$ for HSC 2878. This choice allows the algorithm to remain sensitive to small-scale local overdensities while mitigating the impact of field-star contamination. A total of 100 iterations were performed to ensure the statistical robustness of the membership assignments.

Stars satisfying the conditions of membership probability $P \geq 50\%$, confinement within the cluster's limiting radius, and adherence to the completeness limits were classified as bona fide members. Previous applications of UPMASK have demonstrated its effectiveness in reliably distinguishing true OC members from field contaminants (e.g., Cantat-Gaudin et al., 2020; Yontan et al., 2015, 2022; Yontan, 2023; Yontan & Canbay, 2023; Taşdemir & Yontan, 2023; Taşdemir & Çınar, 2025), and it continues to represent a cornerstone method for OC membership studies.

3.1. Structural and Astrometric Parameters

We applied the UPMASK algorithm to identify the central positions of HSC 25, HSC 37, and HSC 2878 in this study (Cantat-Gaudin et al., 2020). The cluster centres were determined using a two-dimensional Kernel Density Estimation (KDE) technique applied to the spatial distribution of the probable members. Prior to the analysis, the data were subjected to strict astrometric and photometric quality filters (e.g., $\sigma_\varpi/\varpi \leq 0.2$, proper motion error ≤ 0.5 mas yr $^{-1}$, and the corrected $G_{\text{BP}}/G_{\text{RP}}$ excess factor consistency check following Riello et al. (2021)). We employed a Gaussian kernel to estimate the probability density function of the stellar positions. To determine the optimal smoothing parameter, we adopted a bandwidth calculated via Scott's rule, which effectively highlights the density peaks while suppressing background noise. The cluster centre was identified as the location of the maximum stellar density peak. Figure 1 displays the resulting density contours and the distribution of our members (blue filled circles). In this figure, the determined centres are marked by the intersection of vertical and horizontal blue

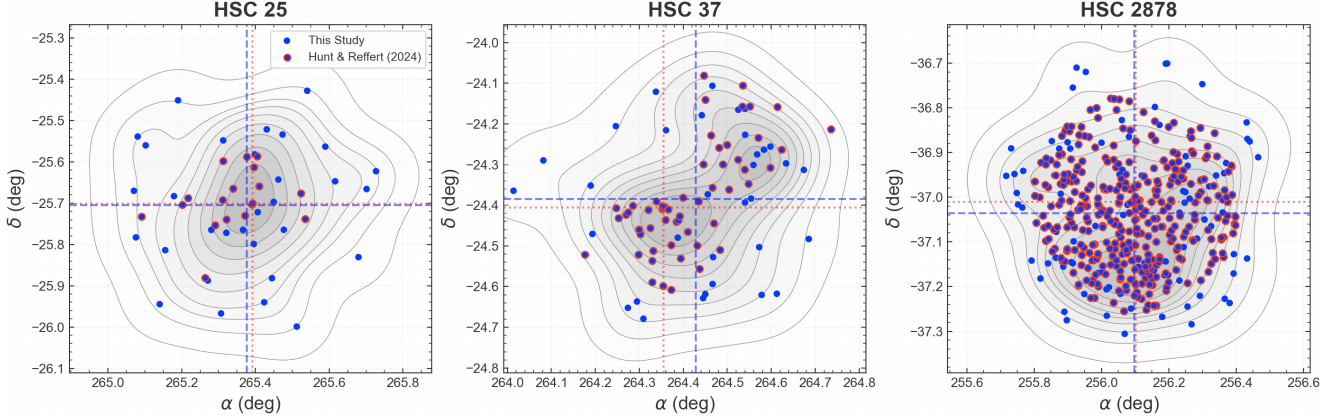


Figure 1: Spatial distribution of probable members for HSC 25, HSC 37, and HSC 2878. The underlying grey contours depict the stellar density levels derived via Kernel Density Estimation (KDE) based on *Gaia* DR3 data. Blue-filled circles represent the members identified in this study, while red open circles indicate the members adopted from Hunt & Reffert (2024). The cluster centres are marked by the intersection of vertical and horizontal lines: blue dashed lines correspond to the centres determined in this work, and red dotted lines represent the coordinates given by Hunt & Reffert (2024).

Table 2: The revised central positions of the OCs have been derived with improved precision and are reported in both equatorial coordinates (α, δ) and Galactic coordinates (l, b).

Cluster	α	δ	l	b
HSC 25	17 ^h 41 ^m 12 ^s .00	-25° 41' 24"	2°.598	1°.934
HSC 37	17 ^h 37 ^m 38 ^s .40	-24° 23' 24"	3°.274	3°.307
HSC 2878	17 ^h 04 ^m 21 ^s .60	-37° 00' 54"	348°.819	2°.034

dashed lines. For comparison, the members and central coordinates reported by Hunt & Reffert (2024) are indicated by red open circles and intersecting red dotted lines, respectively. The resulting coordinate values show strong agreement with the literature and are listed in Table 2.

To characterise the structural properties of the OCs, we constructed radial density profiles (RDPs) by measuring the stellar surface density in concentric annuli around the cluster centres. The observed RDPs were fitted with the empirical King density profile (King, 1962), expressed as:

$$\rho(r) = \rho_{\text{bg}} + \rho_0 \left[\frac{1}{\sqrt{1 + (r/r_c)^2}} - \frac{1}{\sqrt{1 + (r_t/r_c)^2}} \right]^2, \quad (1)$$

where ρ_0 represents the central stellar density, ρ_{bg} is the background density, r_c is the core radius, and r_t is the tidal radius. The fitting process was performed using the weighted least-squares minimization method, where the uncertainties of individual density points were incorporated as weights ($w_i = 1/\sigma_i^2$) to provide a more realistic estimation of the parameter errors and confidence intervals.

The core radii (r_c) for HSC 25, HSC 37 and HSC 2878 were estimated as 5.98 ± 1.56 , 4.22 ± 2.54 , and 7.30 ± 3.11 arcmin, respectively. In addition, the limiting radii (r_{cl}), defined as the radial distance at which the cluster density merges with the background level, were determined to be 10.09 ± 3.66 arcmin for HSC 25, 7.44 ± 3.14 arcmin

Table 3: The structural parameters of the investigated OCs were determined by fitting the observed surface stellar density profiles with King models. This approach enables the estimation of key parameters such as the core, limiting, and central density, offering insights into the internal structure and dynamical state of the OCs.

Parameters	HSC 25	HSC 37	HSC 2878
r_c (arcmin)	5.98 ± 1.56	4.22 ± 2.54	7.30 ± 3.11
r_c (pc)	22.32 ± 5.43	11.80 ± 3.96	19.66 ± 5.09
r_{cl} (arcmin)	10.09 ± 3.66	7.44 ± 3.14	13.54 ± 4.23
r_{cl} (pc)	37.64 ± 7.06	20.81 ± 5.24	36.47 ± 6.95
ρ_o (stars arcmin $^{-2}$)	34.20 ± 5.58	30.67 ± 8.67	22.95 ± 3.06
ρ_{bg} (stars arcmin $^{-2}$)	15.08 ± 0.82	7.66 ± 0.52	8.92 ± 0.26
δ_c	3.27 ± 0.56	5.01 ± 1.46	3.57 ± 0.48
C	1.69 ± 0.54	1.76 ± 0.78	1.85 ± 0.70

for HSC 37, and 13.54 ± 4.23 arcmin for HSC 2878. The central stellar densities (ρ_o) were derived as 34.20 ± 5.58 stars arcmin $^{-2}$ for HSC 25, 30.67 ± 8.67 stars arcmin $^{-2}$ for HSC 37, and 22.95 ± 3.06 stars arcmin $^{-2}$ for HSC 2878. Correspondingly, the background stellar densities (ρ_{bg}) were measured as 15.08 ± 0.82 stars arcmin $^{-2}$, 7.66 ± 0.52 stars arcmin $^{-2}$, and 8.92 ± 0.26 stars arcmin $^{-2}$, respectively.

To further assess the concentration and density enhancement of the OCs, we computed the density contrast parameter (δ_c) and the concentration parameter (C). The density contrast, defined by $\delta_c = 1 + \rho_o / \rho_{\text{bg}}$, quantifies the degree of cluster overdensity relative to the background field. The resulting values of δ_c are 3.27 ± 0.56 for HSC 25, 5.01 ± 1.46 for HSC 37, and 3.57 ± 0.48 for HSC 2878, suggesting significant central concentrations. The concentration parameters, calculated as $C = r_{\text{cl}}/r_c$ (King, 1966), were determined as 1.69 ± 0.54 for HSC 25, 1.76 ± 0.78 for HSC 37, and 1.85 ± 0.70 for HSC 2878, indicating that the OCs possess relatively loose but distinct cores. The results of the King profile fitting applied to each open cluster are presented graphically in Figure 2, while the derived struc-

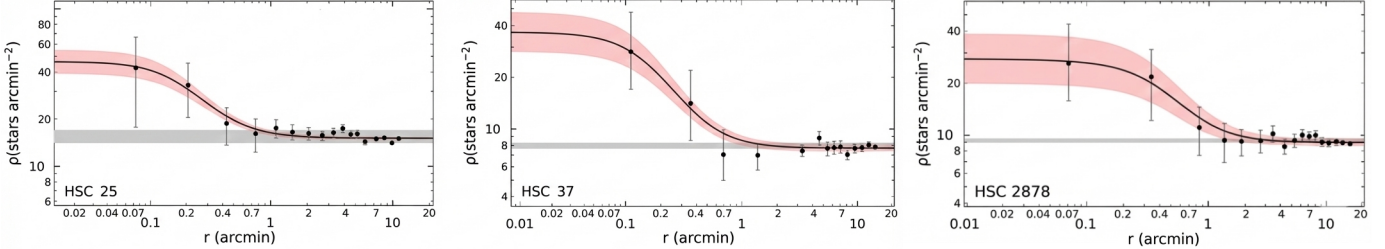


Figure 2: The King profile fitting to the surface density extracted RDP parameters. The solid curve represents the best-fit empirical King profile, calculated by weighting the data points with their errors. The red-shaded band corresponds to the 1σ confidence interval of the fit.

tural parameters are summarised in Table 3.

To investigate the kinematic properties of the clusters HSC 25, HSC 37, and HSC 2878, we constructed vector-point diagrams (VPDs) by plotting the proper-motion components $(\mu_\alpha \cos \delta, \mu_\delta)$ of the member stars. As shown in the upper panels of Figure 3, the mean proper-motion components of each cluster are indicated by blue dashed lines. These values were computed using stars identified as members based on their astrometric consistency. The VPDs provide a visual representation of the clusters' kinematic distributions and support the estimation of their systemic motion. The derived mean proper-motion components for each cluster are listed in Table 4.

The trigonometric parallaxes of the three open clusters analysed in this study were determined using *Gaia* DR3 data by selecting member stars with relative trigonometric parallax uncertainties satisfying $\sigma_\varpi/\varpi \leq 0.2$. These stars were plotted on a parallax-magnitude (ϖ vs. G) diagram, as displayed in Figure 4, to assess the internal consistency of their distances. All selected stars have well-constrained trigonometric parallaxes and magnitudes brighter than $G = 19.5$. The clustering of points around a narrow trigonometric parallax range in each diagram supports their physical association.

Although the trigonometric parallax uncertainties are relatively large at the distances of the studied open clusters, the trigonometric parallaxes of the selected member stars remain within one standard deviation of the cluster mean, in line with the expected *Gaia* DR3 measurement uncertainties. This reflects the internal consistency of the adopted member sample and the effectiveness of the membership selection in minimizing field-star contamination (via the UPMASK algorithm and astrometric quality cuts), rather than any improvement in the intrinsic precision of the parallax measurements.

The mean distances of the clusters were derived by inverting the individual *Gaia* DR3 parallaxes (ϖ_i) of the member stars ($d_i = 1000/\varpi_i$, with ϖ in milliarcseconds). To estimate the internal uncertainty of the mean distance, we computed the error of the weighted mean as follows:

$$\bar{d} = \frac{\sum_i w_i d_i}{\sum_i w_i}, \quad \sigma_{\text{int}} = \left(\sum_i w_i \right)^{-1/2}, \quad (2)$$

where the weights are defined by $w_i = 1/\sigma_i^2$, and σ_i is the uncertainty in each individual distance d_i . Since each distance is computed by inverting the parallax, the uncertainty is propagated accordingly using:

$$\sigma_i = \frac{1000 \cdot \sigma_\varpi}{\varpi_i^2}. \quad (3)$$

To account for the actual spread of the distances among the cluster members, the external uncertainty was estimated using the weighted standard deviation:

$$\sigma_{\text{ext}} = \sqrt{\frac{\sum_i w_i (d_i - \bar{d})^2}{\sum_i w_i}}. \quad (4)$$

The mean trigonometric parallaxes (ϖ) of the cluster members were computed by taking the weighted mean of individual *Gaia* DR3 measurements. The median values and their internal uncertainties are found to be 0.079 ± 0.016 mas for HSC 25, 0.104 ± 0.013 mas for HSC 37, and 0.108 ± 0.010 mas for HSC 2878. These values were converted into distances using the simple inversion formula $d(\text{pc}) = 1000/\varpi$, where ϖ is given in milliarcseconds (mas). Accordingly, the mean distances were estimated as 12.82 ± 2.64 kpc for HSC 25, 9.62 ± 1.19 kpc for HSC 37, and 9.26 ± 0.86 kpc for HSC 2878.

3.2. Photometric Analysis: Reddening, Distance and Age

In the determination of fundamental astrophysical properties of OCs, colour-magnitude diagrams (CMDs) play a pivotal role. These diagrams allow for the identification of principal evolutionary features such as the main sequence (MS), the turn-off point, and evolved stellar populations, which are critical for constraining cluster parameters. In this study, we constructed CMDs for the most probable members ($P \geq 0.5$) of HSC 25, HSC 37, and HSC 2878 using *Gaia* photometric data. The OCs parameters, namely age, distance modulus, reddening, and metallicity, were derived by fitting PARSEC isochrones (Bressan et al., 2012), calibrated for the *Gaia* Early Data Release 3 (EDR3) photometric system (Riello et al., 2021; Gaia Collaboration et al., 2021).

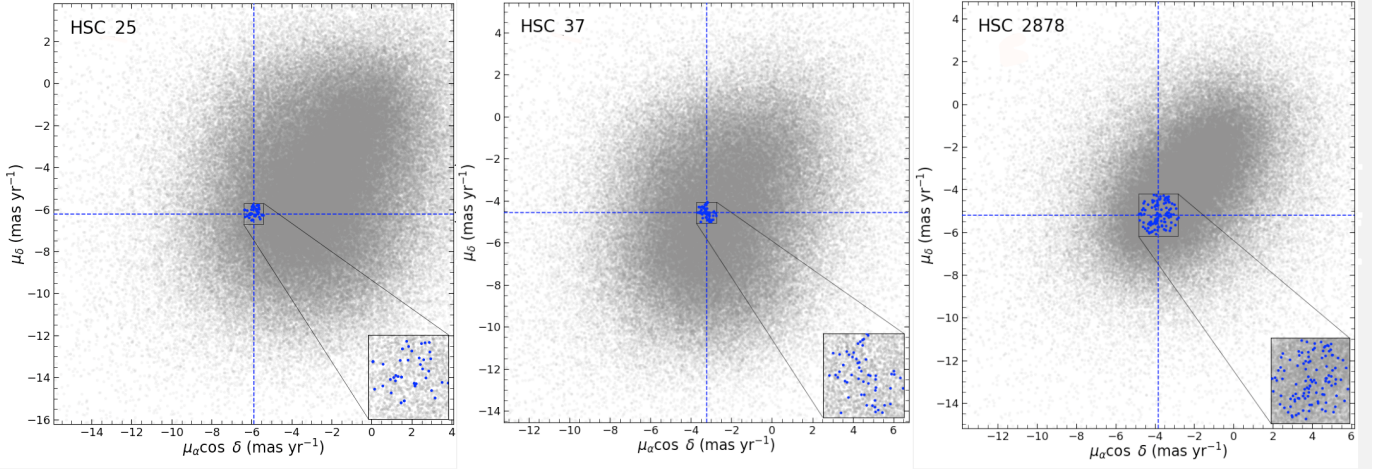


Figure 3: Distributions of the mean proper-motion components ($\mu_\alpha \cos \delta$ and μ_δ) for the candidate OCs members.

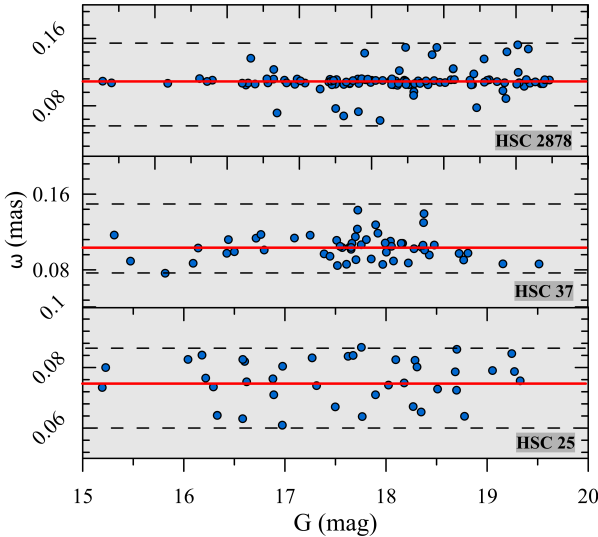


Figure 4: Distribution of member stars for HSC 25, HSC 37, and HSC 2878 in the trigonometric parallax (ω) versus *Gaia* G -band magnitude diagram. The solid red line shows the median parallax value, and the surrounding black dashed lines show the range of values that fall within one standard deviation of the median.

3.2.1. Breaking the Distance–Reddening Degeneracy

The Galactic centre region is heavily affected by interstellar dust and gas, leading to significant line-of-sight extinction and reddening. This effect becomes increasingly prominent for stellar populations located at low Galactic latitudes, where the dust column density is high due to the integrated contribution along the line of sight. OCs such as HSC 25, HSC 37, and HSC 2878, which lie in proximity to the Galactic bulge, are particularly impacted by this phenomenon. In such regions, failure to properly correct for reddening introduces substantial uncertainties in the derivation of fundamental cluster parameters such as distance, age, and metallicity. The degeneracy between distance and extinction can severely bias the results of isochrone fitting and stellar population analysis.

To mitigate this degeneracy, we adopted the distance estimates provided by Bailer-Jones et al. (2021), who constructed a probabilistic distance catalogue for all stars in *Gaia* EDR3 (Riello et al., 2021; Gaia Collaboration et al., 2021). Their method accounts for the asymmetric and non-Gaussian nature of trigonometric parallax uncertainties, especially at small parallaxes, by applying a Bayesian inference framework with a geometric prior based on a spatial density model of the Galaxy. The catalogue offers posterior probability distributions of geometric distances for each star. In this study, we queried the distances of all confirmed member stars of OCs from this catalogue. These distances were combined for the cluster members to construct histograms of the distance distributions, as shown in Figure 5. A Gaussian function was fitted to each histogram to determine the mean OC distances, while the red shaded regions in the figure indicate the corresponding 1σ uncertainties derived from the fits.

Subsequently, for each member star, we retrieved the line-of-sight total visual extinction value, $A_{\infty(V)}$, from the IRSA Galactic Dust Reddening and Extinction Service¹. This service is based on the dust maps of Schlegel, Finkbeiner, & Davis (1998), with updated extinction coefficients from Schlafly & Finkbeiner (2011), and provides the integrated extinction assuming infinite distance. To derive the extinction appropriate for the actual distance of each star, we applied a vertical dust distribution model using the expression:

$$A_d(V) = A_{\infty(V)} \left[1 - \exp\left(\frac{-|d \times \sin(b)|}{H}\right) \right]. \quad (5)$$

where, d is the heliocentric distance from Bailer-Jones et al. (2021) and b denotes the Galactic latitude. The interstellar dust distribution is modelled with a scale height (H) of ± 125 pc following Marshall et al. (2006). We distinguished between the total dust absorption along the line

¹<https://irsa.ipac.caltech.edu/applications/DUST/>

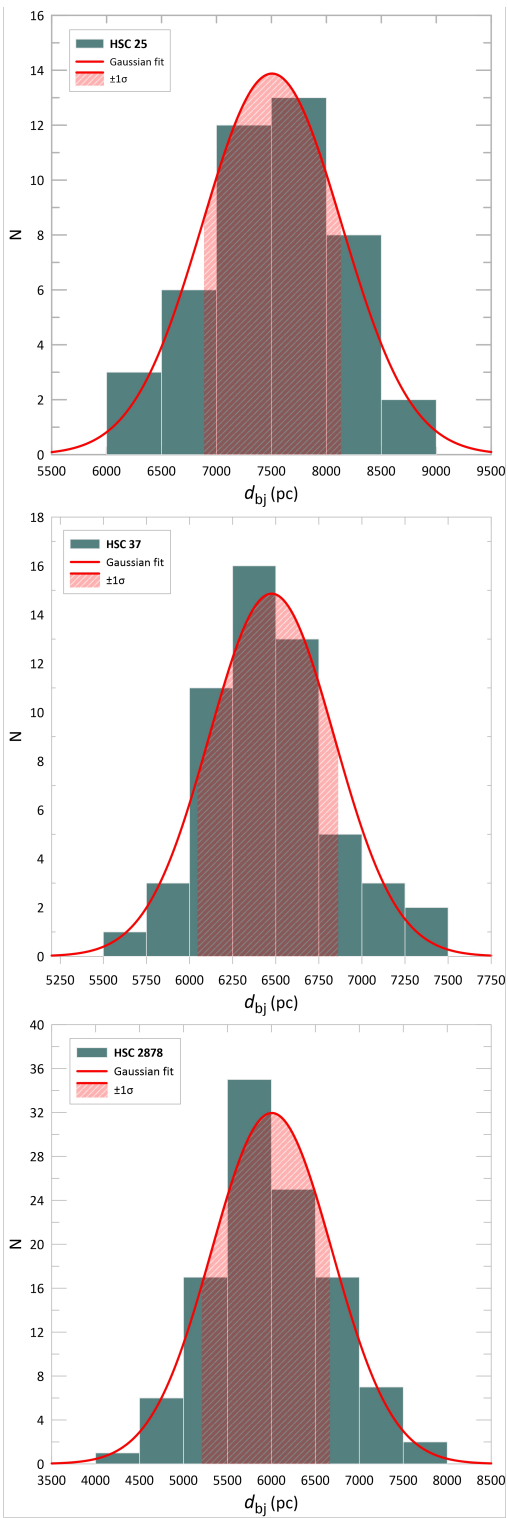


Figure 5: Distance distributions of member stars in the clusters HSC 25, HSC 37, and HSC 2878 based on their individual Bailer-Jones distances (d_{BJ}). The histograms represent the estimated distance values, while the red curve indicates the Gaussian fit applied to the distributions. The shaded region shows the $\pm 1\sigma$ range around the mean, corresponding to the internal uncertainty.

of sight, $A_{\infty}(V)$, and the absorption up to the star's distance, $A_d(V)$, as defined in previous studies (Bilir, Güver, & Aslan, 2006; Bilir et al., 2008a,b; Bostancı et al., 2015, 2018). Applying this correction yielded a set of extinction values for each cluster member. As illustrated in Figure 6, each cluster exhibits noticeable differential reddening. As expected, the reddening values tend to increase toward the Galactic centre direction, reflecting the higher concentration of interstellar dust along these sightlines.

To convert visual extinction into *Gaia* photometric system quantities, we adopted the total-to-selective extinction law of Cardelli, Clayton, & Mathis (1989), which provides band-dependent extinction coefficients based on a standard reddening law with $R_V = 3.1$. Specifically, the following selective extinction ratios were used, consistent with the *Gaia* DR3 photometric response: $A_G/A_V = 0.83627$, $A_{G_{\text{BP}}}/A_V = 1.08337$, and $A_{G_{\text{RP}}}/A_V = 0.63439$ (Canbay et al., 2023, see also). The *Gaia* colour excess $E(G_{\text{BP}} - G_{\text{RP}})$ was then estimated using the empirical relation:

$$E(G_{\text{BP}} - G_{\text{RP}}) = \frac{A_G}{1.8626}, \quad (6)$$

where A_G denotes the extinction in the *Gaia* G -band, computed from the relation $A_G = 0.83627 \times A_V$. This transformation enabled the determination of individual reddening values in *Gaia* colours for each cluster member, which were subsequently incorporated into the isochrone fitting procedure. As a result of this procedure, A_V values for HSC 25, HSC 37, and HSC 2878 were estimated to be 4.43 ± 0.29 , 2.93 ± 0.29 , and 3.41 ± 0.41 mag, respectively. Using the adopted extinction transformations, $E(G_{\text{BP}} - G_{\text{RP}})$ were calculated as 1.99 ± 0.13 , 1.32 ± 0.13 , and 1.54 ± 0.18 mag, respectively. Taking into account that each cluster member may be affected by differential reddening, we adopted individual reddening values for each star and incorporated them accordingly in the isochrone fitting analysis.

The CMDs in the $G \times (G_{\text{BP}} - G_{\text{RP}})$ plane were used to perform the isochrone fitting for each cluster, focusing on the most reliable stellar members. A visual fitting method was adopted, emphasising the alignment of the isochrones with the observed MS and evolved stars (Bisht et al., 2022, ?, 2026). Prior to fitting, the metallicity $[\text{Fe}/\text{H}]$ of each cluster was converted into the mass fraction z by employing the analytic relations provided by Bovy² for PARSEC models:

$$z_x = 10^{[\text{Fe}/\text{H}]} \times \left(\frac{z_{\odot}}{1 - 0.248 - 2.78 \times z_{\odot}} \right), \quad (7)$$

$$z = \frac{z_x - 0.2485 \times z_x}{2.78 \times z_x + 1}.$$

where the adopted solar metallicity is $z_{\odot} = 0.0152$ (Bressan et al., 2012). For HSC 25, HSC 37, and HSC 2878, the metallicities were determined as $z = 0.0388 \pm$

²<https://github.com/jobovy/isodist/blob/master/isodist/Isochrone.py>

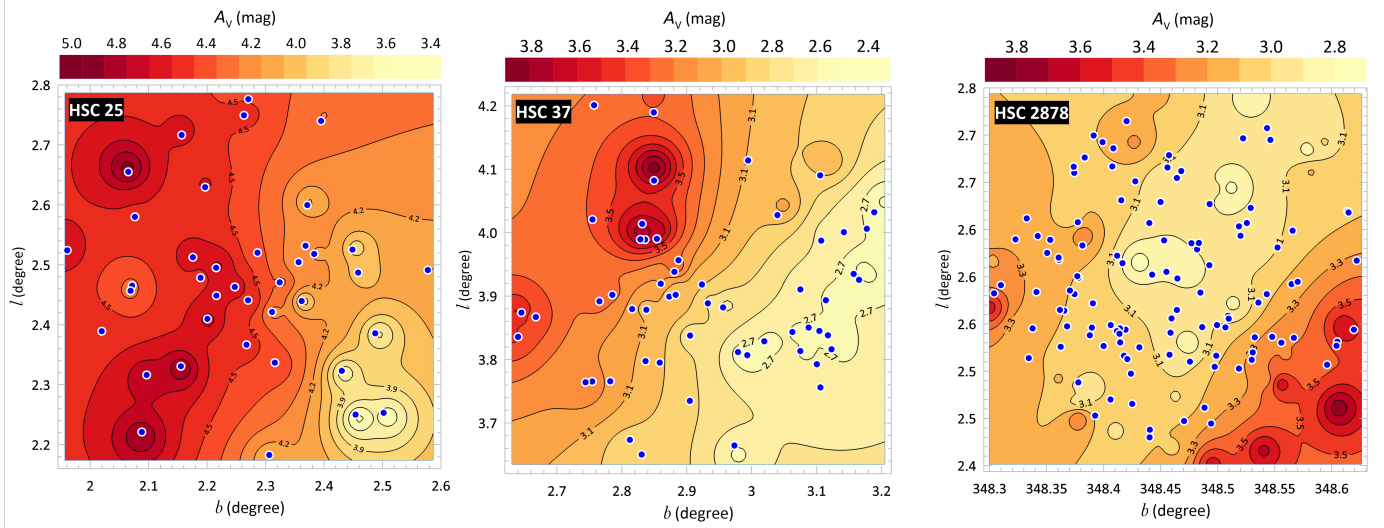


Figure 6: V -band extinction (A_V) contour maps for the fields centred on the clusters HSC 25 (left), HSC 37 (middle), and HSC 2878 (right). The extinction values are interpolated from Schlafly & Finkbeiner (2011) dust maps using the IRSAs interface. Blue points indicate the positions of member stars. These A_V values have been rescaled according to the individual Bailer-Jones et al. (2021) geometric distances of the stars in each OCs field.

0.0039 , 0.0259 ± 0.0028 , and 0.0209 ± 0.0023 , respectively. Isochrone fitting yielded OCs ages of $\log(t/\text{yr}) = 8.38 \pm 0.08$ for HSC 25, $\log(t/\text{yr}) = 7.04 \pm 0.09$ for HSC 37, and $\log(t/\text{yr}) = 9.04 \pm 0.09$ for HSC 2878.

From the isochrone fitting, the distance moduli were derived as $(m - M) = 18.04 \pm 0.09$ mag for HSC 25, 16.62 ± 0.06 mag for HSC 37, and 16.82 ± 0.08 mag for HSC 2878, corresponding to distances of 7.36 ± 0.37 , 6.79 ± 0.18 , and 6.17 ± 0.22 kpc, respectively. All obtained fundamental astrometric and astrophysical parameters within HSC 25, HSC 37, and HSC 2878 are listed here with Table 4. The spectral type classes (Pecaut & Mamajek, 2013) shown in Figure 7, the pre-MS region is visible before the early F-type stars and indicates the stage at which these stars reach the MS for HSC 37. Although the CMD has been corrected for the line-of-sight reddening, the stars in this evolutionary phase are still embedded in a relatively dusty environment. This residual internal extinction, likely associated with the cluster's natal material, is still discernible in the CMD as a slight colour excess among the pre-MS members.

The isochrone distances are in general agreement with those derived from the mean distances of Bailer-Jones et al. (2021), yielding $d_{\text{BJ}} = 7.51 \pm 2.35$ kpc for HSC 25, 6.46 ± 2.92 kpc for HSC 37, and 5.94 ± 2.42 kpc for HSC 2878. However, a noticeable discrepancy is observed for HSC 25, where the trigonometric parallax-based distance exceeds the isochrone distance. This difference can plausibly be attributed to the significant interstellar reddening effects associated with the proximity of HSC 25 to the Galactic centre, which may lead to an overestimation of distances when relying solely on trigonometric parallax measurements.

To explore the spatial distribution of the OCs within

the MW, the Galactocentric distance (R_{gc}) was computed using the following formula:

$$R_{\text{gc}} = \sqrt{R_0^2 + d^2 \cos^2 b - 2R_0 d \cos b \cos l} \quad (8)$$

where R_{\odot} is the distance from the Sun to the Galactic centre set at $R_{\text{gc}} = 8$ kpc (Bovy & Tremaine, 2012; Bovy, 2015), d is the distance to the cluster, and l and b represent the Galactic longitude and latitude, respectively. In addition, the Galactocentric Cartesian coordinates $(X, Y, Z)_{\odot}$ for each cluster were calculated. In this context, the vector X is directed towards the Galactic centre, Y towards the direction of Galactic rotation, and Z towards the Galactic north pole. The resulting positions for HSC 25, HSC 37, and HSC 2878 are listed in Table 4.

Furthermore, the Galactocentric distances were calculated as $R_{\text{gc}} = 0.76 \pm 0.25$ kpc for HSC 25, 1.92 ± 0.09 kpc for HSC 37, and 1.86 ± 0.21 kpc for HSC 2878. Compared to the values reported by Hunt & Reffert (2024), HSC 25 and HSC 2878 are found to be closer to the Galactic centre, while HSC 37 appears slightly farther.

3.3. Dynamical and Kinematical Structure

The dynamical and kinematical characterisation of OCs are essential for understanding their formation, evolution, and interaction with the Galactic environment. The internal dynamical state reflects processes such as mass segregation, energy equipartition, and tidal stripping, while the kinematical properties provide critical information about the OCs' origins and their trajectories within the MW. By examining relaxation times, space velocities, Solar motion components, and orbital parameters, it is possible to reconstruct the dynamical histories of OCs and infer their membership in distinct Galactic populations. Such analyses contribute not only to the detailed mapping of the

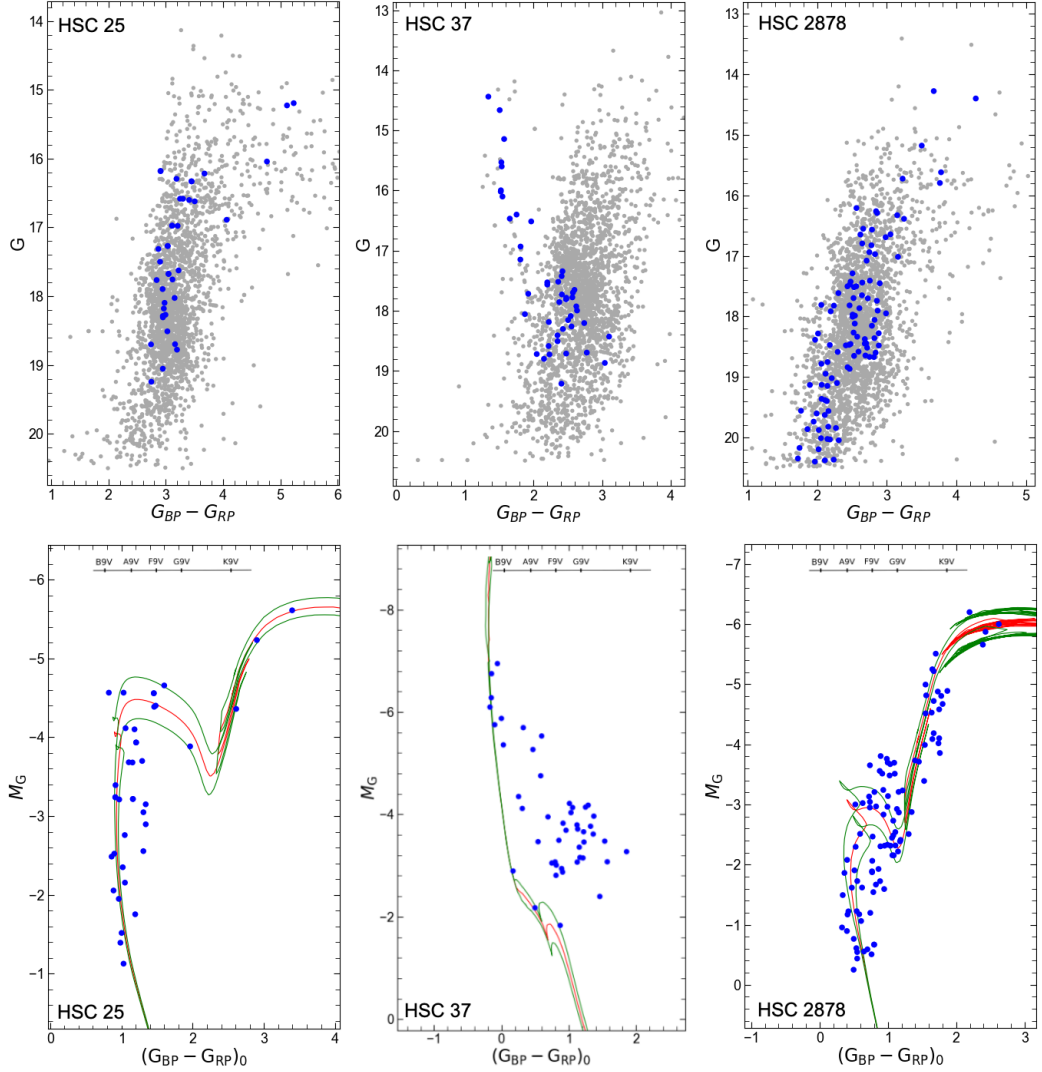


Figure 7: colour–magnitude diagrams (CMDs) for the clusters HSC 25, HSC 37, and HSC 2878. Top row: Observed G versus $(G_{BP} - G_{RP})_0$ distributions including both member (blue) and field stars (gray), without correction for interstellar reddening. Bottom row: Reddening-corrected CMDs showing absolute magnitude M_G versus intrinsic colour $(G_{BP} - G_{RP})_0$ for the same clusters. The red curves represent the best-fitting PARSEC isochrones, whereas the surrounding green curves delineate the uncertainty bounds associated with the fitting process.

Galactic structure but also to the broader understanding of star cluster evolution under the influence of external gravitational perturbations.

3.3.1. The Dynamical Relaxation Time

The Luminosity Function (LF) is a useful tool for examining the distribution of stellar brightness within a cluster, expressed as the number of stars per absolute magnitude interval (Haroon et al., 2017). In this study, G -band LFs were constructed for stars with absolute magnitudes derived from the reddening-corrected distance moduli $(m - M)_0$ determined for each OC, and are shown in Figure 8.

Due to the limited number of main-sequence (MS) stars in HSC 2878 and the insufficient MS population in HSC 25 and HSC 37, a reliable slope determination for the Initial Mass Function (IMF) could not be performed. Therefore,

stellar masses were estimated on a star-by-star basis using the mass–luminosity relations provided by the best-fitting isochrones. For each high-probability member star, the reddening-corrected absolute magnitudes and colours were matched to the corresponding points along the isochrone, and the stellar mass was directly assigned. For evolved stars, individual masses were inferred according to their evolutionary stage on the isochrones.

Using this approach, we obtained observed stellar masses of approximately $135, M_\odot$ for HSC 25, $755, M_\odot$ for HSC 37, and $204, M_\odot$ for HSC 2878, including both main-sequence and evolved members. These values represent the observed cluster masses, derived solely from the confirmed member stars, without any extrapolation toward lower, unobserved stellar masses. A summary of the derived parameters, including the observed cluster mass (M_{obs}) and the mean stellar mass $\langle M \rangle$, is given in Table 5.

Table 4: A detailed comparison of the astrophysical and photometric properties determined for HSC 25, HSC 37, and HSC 2878 within the scope of this investigation is presented.

Parameters	HSC 25	HSC 37	HSC 2878
No. of members	44	55	112
Astrometric Parameters			
$\mu_\alpha \cos \delta$ (mas yr $^{-1}$)	-5.901 ± 0.41	-3.231 ± 0.56	-3.830 ± 0.51
μ_δ (mas yr $^{-1}$)	-6.213 ± 0.40	-4.564 ± 0.47	-5.198 ± 0.44
ϖ (mas)	0.079 ± 0.016	0.104 ± 0.013	0.108 ± 0.010
d_ϖ (kpc)	12.82 ± 2.64	9.62 ± 1.19	9.26 ± 0.86
d_{BJ} (kpc)	7.51 ± 2.35	6.46 ± 2.92	5.94 ± 2.42
Astrophysical Parameters			
A_V (mag)	4.43 ± 0.29	2.93 ± 0.29	3.41 ± 0.41
$E(B - V)$ (mag)	1.41 ± 0.09	0.94 ± 0.09	1.09 ± 0.13
$E(G_{\text{BP}} - G_{\text{RP}})$ (mag)	1.99 ± 0.13	1.32 ± 0.13	1.54 ± 0.18
d_{iso} (kpc)	7.36 ± 0.37	6.79 ± 0.18	6.17 ± 0.22
$(m - M)$ (mag)	18.04 ± 0.09	16.62 ± 0.06	16.82 ± 0.08
Z	0.0388 ± 0.0039	0.0259 ± 0.0028	0.0209 ± 0.0023
$\log(t/\text{yr})$	8.38 ± 0.08	7.04 ± 0.09	9.04 ± 0.09
X_\odot (kpc)	7.33 ± 0.34	6.64 ± 0.18	6.16 ± 0.22
Y_\odot (kpc)	0.37 ± 0.02	-1.36 ± 0.04	0.25 ± 0.01
Z_\odot (kpc)	0.51 ± 0.02	0.31 ± 0.01	0.27 ± 0.01
R_{gc} (kpc)	0.76 ± 0.25	1.92 ± 0.09	1.86 ± 0.21

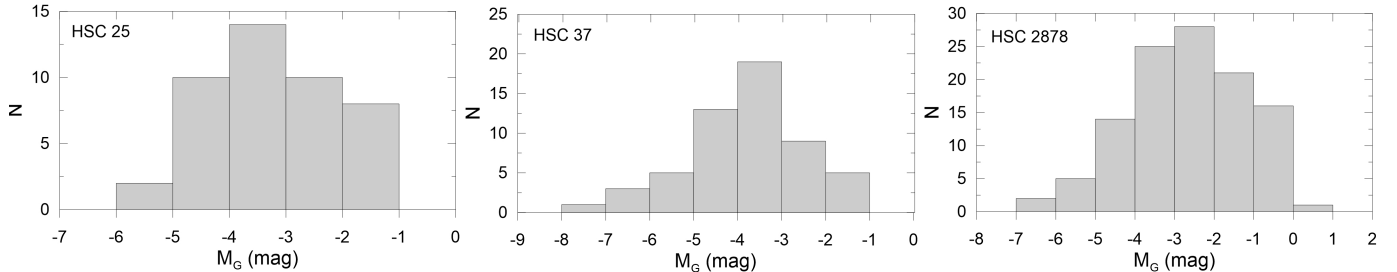


Figure 8: The luminosity function frequency distributions in the absolute magnitude G -band (M_G) have been derived for the three OCs examined in this study.

The dynamical relaxation time (T_{relax}) characterises the period required for a star cluster to reach dynamical equilibrium, where the internal stellar motions balance the competing processes of contraction and potential disruption. Estimating this timescale is essential for assessing the dynamical maturity of a cluster, revealing whether it has achieved a stable configuration or remains dynamically young (Haroon et al., 2017). A short T_{relax} implies that the cluster has undergone significant internal dynamical evolution, whereas a long T_{relax} suggests a less dynamically evolved system.

Following the prescription of Spitzer & Hart (1971), the dynamical relaxation time is calculated using the relation:

$$T_{\text{relax}} = \frac{8.9 \times 10^5 N^{1/2} R_h^{3/2}}{\langle M_C \rangle^{1/2} \log(0.4N)}, \quad (9)$$

where N is the total number of stars in the cluster, $\langle M_C \rangle$ denotes the mean stellar mass, and R_h is the half-mass radius expressed in parsecs. The half-mass radius was derived according to the transformation proposed by Sable-

viciute et al. (2006):

$$R_h = 0.547 \times r_c \times \left(\frac{r_t}{r_c} \right)^{0.486}, \quad (10)$$

where r_c is the core radius and r_t is adopted as the limiting radius r_{cl} , obtained from the cluster RDP as the radius where the fitted King profile meets the background density, following the method described by (Tanik Ozturk et al., 2025). This substitution is commonly employed in cases where the formal tidal radius cannot be robustly constrained observationally. Based on these parameters, the corresponding dynamical relaxation times are estimated as 156 ± 54 Myr for HSC 25, 31 ± 15 Myr for HSC 37, and 214 ± 76 Myr for HSC 2878. It should be noted that the mean stellar mass used in the relaxation time calculation is derived solely from the observed member stars and does not include stars below the detection limit. As a result, the reported T_{relax} values should be regarded as upper limits, since the inclusion of lower-mass stars would reduce the mean stellar mass and lead to shorter relaxation times.

3.3.2. Determination of Galactic Velocity Components

The space-velocity components (V_x , V_y , V_z) for individual stars were derived based on their proper-motion components, radial velocities, and distances utilising the standard relations presented in Haroon et al. (2025a). Radial velocity is a key parameter for accurately reconstructing the orbital trajectories of stellar systems around the Galactic centre. In this study, the mean radial velocities of HSC 25, HSC 37, and HSC 2878 were determined individually. For each cluster, the most probable members with available radial velocity measurements in *Gaia* DR3 were selected, resulting in 2, 5, and 6 stars, respectively. The mean radial velocities were calculated according to the procedure described by Carrera et al. (2022), yielding $V_R = -101.09 \pm 35.72 \text{ km s}^{-1}$ for HSC 25, $V_R = 41.04 \pm 29.08 \text{ km s}^{-1}$ for HSC 37, and $V_R = -124.64 \pm 19.43 \text{ km s}^{-1}$ for HSC 2878. It is worth noting that while the radial velocity of HSC 25 is not provided in the Hunt & Reffert (2024) catalogue, the radial velocities derived for HSC 37 and HSC 2878 in this work are in good agreement with the values reported therein.

To interpret the kinematics within the Galactic frame, the space velocity vectors were transformed from equatorial to Galactic coordinates (U , V , W), following the transformation matrix outlined by Haroon et al. (2025a). Here, U is defined positive toward the Galactic centre V in the direction of Galactic rotation, and W toward the North Galactic Pole. The mean Galactic space-velocity components (\bar{U} , \bar{V} , \bar{W}) were subsequently obtained by averaging over the OC members. The distributions of individual (U , V , W) components for the OC members are presented in Figure 9, while the computed mean values for each OC are summarised in Table 5.

The estimation of the solar motion components (U_\odot , V_\odot , W_\odot) relies on the Galactic space velocities of well-characterised stellar groups that can act as reference frames for the Sun's kinematics within the MW. In this study, the mean Galactic space-velocity components (\bar{U} , \bar{V} , \bar{W}) obtained for HSC 25, HSC 37, and HSC 2878 were utilised to infer the solar motion parameters.

To investigate the intrinsic space motions of the HSC 25, HSC 37, and HSC 2878 within the Galactic context, we transformed their heliocentric velocity vectors into the Local Standard of Rest (LSR) frame. This transformation corrects for the peculiar motion of the Sun, for which we adopted the values determined by Coşkunoğlu et al. (2011), namely $(U, V, W)_\odot = (8.83 \pm 0.24, 14.19 \pm 0.34, 6.57 \pm 0.21) \text{ km s}^{-1}$. In this convention, U is directed towards the Galactic centre, V follows the direction of Galactic rotation, and W is oriented towards the north Galactic pole.

To further refine the space velocity components, we applied corrections for the differential rotation of the Galaxy using the classical Oort constants A and B . The corrections to the velocity components U and V are given by:

$$\Delta U = -A d \sin(2l) \cos^2 b, \quad (11)$$

$$\Delta V = -A d \cos(2l) \cos^2 b - B d \cos b, \quad (12)$$

where d is the heliocentric distance, and l and b are the Galactic longitude and latitude of the cluster, respectively. We adopted the Oort constants values as $A = 15.3 \pm 0.4 \text{ km s}^{-1} \text{kpc}^{-1}$ and $B = -11.9 \pm 0.4 \text{ km s}^{-1} \text{kpc}^{-1}$ (Feast & Whitelock, 1997). These differential rotation corrections allow us to isolate the intrinsic motions of the clusters relative to the Local Standard of Rest more precisely by removing the systematic effects of Galactic rotation.

The velocity components of the OCs in the LSR frame were calculated by subtracting the solar motion vector from their observed heliocentric velocity vectors. This correction enables an accurate determination of the OCs' motions relative to the mean motion of stars in the Solar neighbourhood. The total space velocity relative to the LSR, denoted as S_{LSR} , is computed from the corrected velocity components using the relation:

$$S_{\text{LSR}} = \sqrt{U_{\text{LSR}}^2 + V_{\text{LSR}}^2 + W_{\text{LSR}}^2}. \quad (13)$$

Applying this formulation, we obtained LSR-relative total space velocities of $S_{\text{LSR}} = 279.23 \pm 21.28 \text{ km s}^{-1}$ for HSC 25, $S_{\text{LSR}} = 151.64 \pm 15.26 \text{ km s}^{-1}$ for HSC 37, and $S_{\text{LSR}} = 225.79 \pm 17.94 \text{ km s}^{-1}$ for HSC 2878. The derived S_{LSR} values for HSC 25, HSC 37, and HSC 2878 are significantly higher than the typical velocities associated with thin-disc stellar populations. Given their positions and kinematics, these open clusters are identified as bulge clusters rather than typical thin-disc members. Their elevated space velocities, exceeding 150 km s^{-1} in all cases, reflect the dynamically hotter environment of the Galactic bulge. Such kinematic signatures imply that these OCs may have originated in a dynamically hotter environment or could be remnants of accreted systems. Their high total velocities support this interpretation and point to a more complex formation or evolutionary history compared to classical young OCs (Leggett, 1992).

3.3.3. Orbit Parameters and Galactic Population

To analyse the orbital characteristics of HSC 25, HSC 37, and HSC 2878, we utilised both axisymmetric and non-axisymmetric gravitational models implemented in the GALPY³ library, a widely adopted Python toolkit for Galactic dynamics studies. As the baseline axisymmetric potential, we adopted MWpotential2014, developed by Bovy (2015), which provides a self-consistent and observationally calibrated model of the Milky Way's gravitational field. This potential comprises three main components: a power-law bulge with an exponential cut-off, a flattened disc following the Miyamoto–Nagai formulation, and a spherical dark matter halo modelled by the Navarro–Frenk–White (NFW) profile.

The total gravitational potential of this axisymmetric model is expressed as

$$\Phi_{\text{total}}(R, z) = \Phi_{\text{bulge}}(r) + \Phi_{\text{disc}}(R, z) + \Phi_{\text{halo}}(r), \quad (14)$$

³<https://galpy.readthedocs.io/en/v1.5.0/>

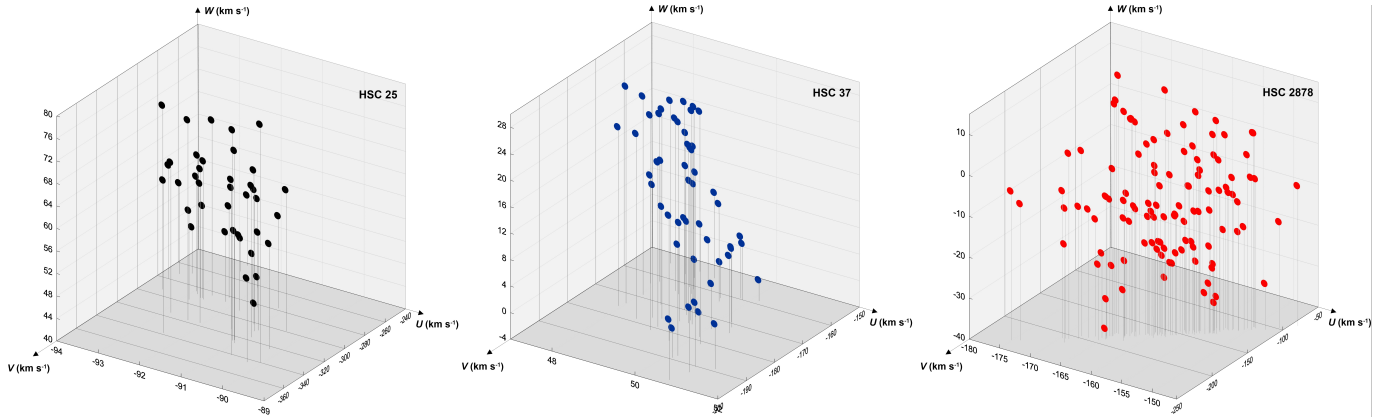


Figure 9: Velocity dispersion profiles of HSC 25, HSC 37, and HSC 2878 projected onto the Galactic coordinate axes, illustrating the distribution of their spatial motion components.

where $r = \sqrt{R^2 + z^2}$ denotes the Galactocentric spherical radius. MWpotential2014 is particularly well-suited for orbit integrations in the outer and intermediate regions of the Galaxy due to its ability to reproduce key observables, such as the Galactic rotation curve and local circular velocity.

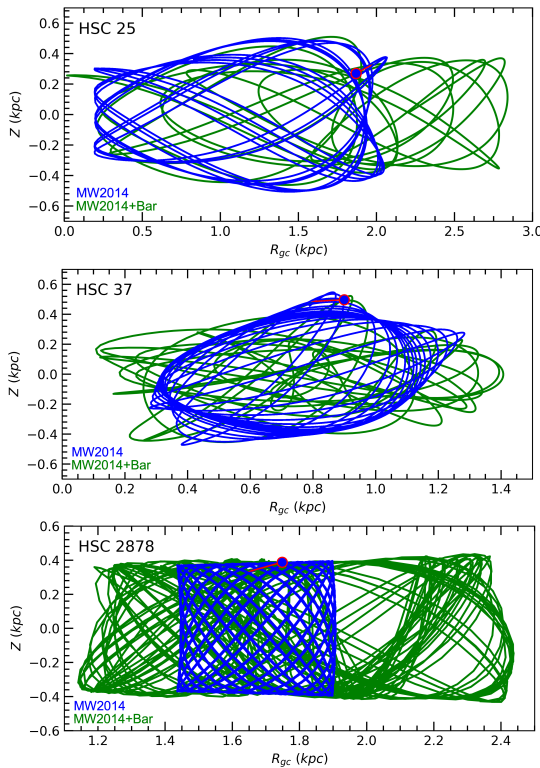


Figure 10: Galactic orbits of HSC 25, HSC 37, and HSC 2878 projected in the Z vs. R_{gc} plane. Blue lines show orbits integrated using the axisymmetric MWpotential2014, while green lines include the additional effect of a non-axisymmetric bar component (DehnenBarPotential). Arrows indicate the direction of motion. The inclusion of the Galactic bar results in noticeable deviations, particularly near perigalactic passages.

However, for objects located in the inner Galaxy ($R_{\text{gc}} <$

2 kpc), the axisymmetric approximation becomes insufficient due to the prominent influence of the Galactic bar. To account for this, we further included the non-axisymmetric DehnenBarPotential, which models the bar as a rotating quadrupole perturbation with time-dependent amplitude. Its potential takes the general form:

$$\Phi_{\text{bar}}(R, \phi, t) = A(t) \cos[2(\phi - \Omega_{\text{bar}}t)] \times f(R), \quad (15)$$

where Ω_{bar} is the bar's pattern speed, and $A(t)$ describes the secular growth of the bar. The radial function $f(R)$ defines how the strength of the perturbation varies across the disc and decays beyond a characteristic bar radius R_{bar} .

In our simulations, we adopted literature-supported parameters with $\Omega_{\text{bar}} = 40 \text{ km s}^{-1} \text{ kpc}^{-1}$, $R_{\text{bar}} = 3.5 \text{ kpc}$, a dimensionless amplitude $\alpha = 0.01$, and a bar orientation angle of 25° relative to the Sun–Galactic centre line (Bland-Hawthorn and Gerhard, 2016; Portail et al., 2017). This composite potential setup allows us to examine the orbital response of clusters located in the dynamically complex inner Galaxy, where the bar can cause significant deviations from circular orbits via resonant trapping, increased eccentricity, or radial migration.

We integrated the orbits of each cluster using both the standard MWpotential2014 model and the extended version that includes the rotating bar potential. The resulting trajectories are displayed in Figures 10 and 11, where differences between the two models become especially pronounced near perigalactic passages.

The orbital calculations were performed by adopting key Galactic parameters: the Sun's circular velocity ($V_{\text{rot}} = 220 \text{ km s}^{-1}$), and its vertical offset from the Galactic plane ($Z_0 = 25 \pm 5 \text{ pc}$) (Juric et al., 2008). These values were chosen to ensure consistency with the structural and kinematical framework described in the Methods section. For each OC, we considered essential astrometric inputs equatorial coordinates (α, δ), heliocentric distances (d), proper-motion components ($\mu_\alpha \cos \delta, \mu_\delta$), and radial velocities (V_r). Based on these parameters, present-day Galactic positions were established, and backwards orbit

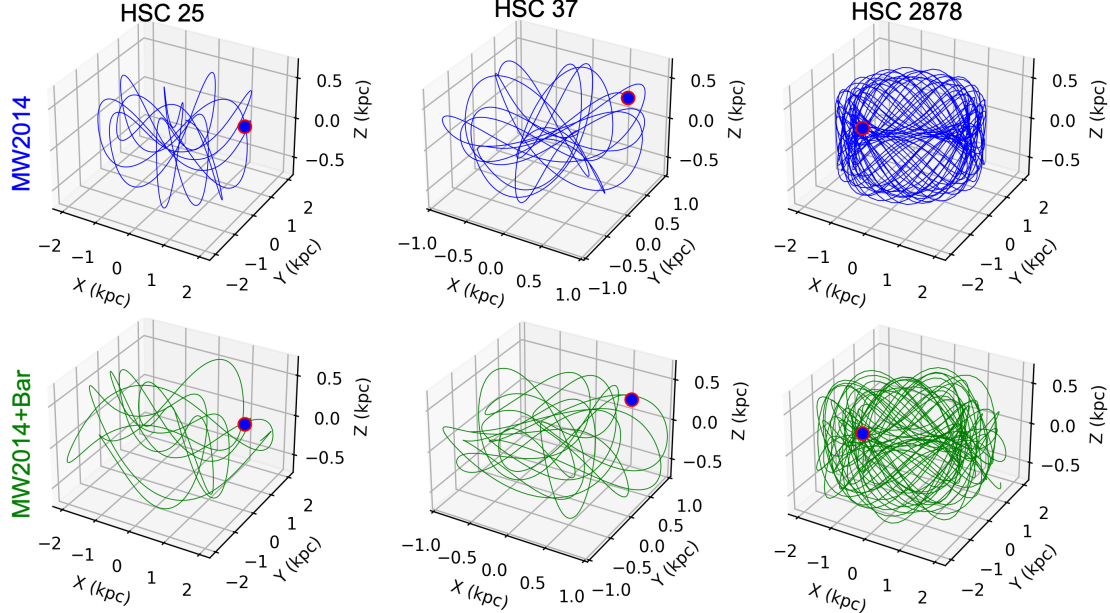


Figure 11: Three-dimensional Galactic orbits of HSC 25, HSC 37, and HSC 2878 shown in the Cartesian (X, Y, Z) coordinate system, centred on the Galactic centre. Blue trajectories correspond to integrations using the axisymmetric `MWPotential2014` while green trajectories include the non-axisymmetric `DehnenBarPotential`. The differences between the two models highlight the bar-induced perturbations in the orbital paths, particularly in the inner Galaxy.

integrations were carried out using a time resolution of 1 Myr, consistent with the OCs' estimated ages (Sahin & Bilir, 2020; Çınar et al., 2025; Canbay et al., 2025).

The orbital simulations, performed under both the axisymmetric `MWPotential2014` model and its non-axisymmetric extension including the `DehnenBarPotential`, are summarized in Table 5 and visualized in Figure 10. For each potential, we report the apogalactic (R_a) and perigalactic (R_p) distances, representing the farthest and closest points of the cluster's orbit relative to the Galactic centre. The parameter Z_{\max} denotes the maximum vertical displacement from the Galactic plane, while the orbital eccentricity, defined as $e = (R_a - R_p)/(R_a + R_p)$, characterises the orbital shape. Additionally, the azimuthal period T_p indicates the time required for a complete orbital revolution around the Galactic centre, serving as a measure of the angular orbital timescale. By comparing results obtained under both potentials, the influence of the Galactic bar on the clusters' orbits is explicitly revealed.

To assess the impact of observational uncertainties on the derived orbital solutions, we performed a Monte Carlo analysis by varying the input velocity components of each OC within their measured uncertainties. For each cluster, multiple orbital integrations were carried out for both the axisymmetric `MWPotential2014` model and the non-axisymmetric configuration, including the `DehnenBarPotential`. The resulting dispersions in the derived orbital parameters (such as R_a , R_p , Z_{\max} , eccentricity, and orbital period) were used to quantify the associated uncertainties. These uncertainty estimates are re-

ported in Table 5, while the corresponding orbital tracks are illustrated in Figures 10 and 11. We find that, although velocity uncertainties slightly broaden the parameter ranges, the overall orbital classifications and qualitative dynamical behaviour of the clusters remain unchanged.

4. Summary and Conclusion

Open clusters located near the Galactic centre remain among the least explored stellar systems due to severe extinction, high stellar densities, and strong dynamical perturbations. In this study, we present a comprehensive analysis of three OCs, HSC 25, HSC 37, and HSC 2878, which rank among the closest known OCs to the Galactic centre and have so far lacked detailed characterisation in the literature.

These systems span a wide range of evolutionary stages, from the very young HSC 37 ($\log(t/\text{yr}) = 7.04$), through the intermediate-age HSC 25 ($\log(t/\text{yr}) = 8.38$), to the older HSC 2878 ($\log(t/\text{yr}) = 9.04$), providing a rare opportunity to investigate the age-dependent properties of OCs in the innermost disc. This chronological diversity enables a more comprehensive examination of cluster evolution under the extreme environmental conditions near the Galactic centre. Considering the metallicities of the clusters, their chemical enrichment supports complex formation histories within the Galactic bulge. Binary merger events and other dynamical interactions can enhance metal abundances while also influencing cluster properties such as age dispersion and stellar population characteristics (e.g., Molero et al., 2024).

Table 5: The evolving, kinematical, and dynamical parameters for the HSC 25, HSC 37, and HSC 2878 OCs.

Parameter	HSC 25	HSC 37	HSC 2878
Dynamical Parameters			
R_h (pc)	15.74 ± 3.39	8.50 ± 2.51	14.52 ± 3.28
T_{relax} (Myr)	156 ± 54	31 ± 15	214 ± 76
M_C (M_\odot)	135	755	204
$\langle M_C \rangle$ (M_\odot)	3.56	15.32	2.17
Kinematical Parameters			
V_R (km s $^{-1}$)	-101.09 ± 35.72	41.04 ± 29.08	-124.64 ± 19.43
$\overline{V_x}$ (km s $^{-1}$)	-193.80 ± 13.92	-96.78 ± 9.84	-60.23 ± 7.76
$\overline{V_y}$ (km s $^{-1}$)	202.40 ± 14.23	30.23 ± 5.50	209.30 ± 14.47
$\overline{V_z}$ (km s $^{-1}$)	-153.54 ± 12.40	-145.03 ± 12.04	-43.15 ± 6.57
\overline{U} (km s $^{-1}$)	-91.81 ± 9.58	49.19 ± 7.01	-158.44 ± 12.59
\overline{V} (km s $^{-1}$)	-299.92 ± 17.32	-169.41 ± 13.02	-155.33 ± 12.46
\overline{W} (km s $^{-1}$)	60.91 ± 7.81	13.88 ± 3.73	-7.83 ± 2.80
U_{LSR} (km s $^{-1}$)	-73.85 ± 9.58	67.90 ± 7.01	-185.64 ± 12.59
V_{LSR} (km s $^{-1}$)	-260.69 ± 17.32	-134.04 ± 13.02	-128.52 ± 12.47
W_{LSR} (km s $^{-1}$)	67.48 ± 7.81	20.45 ± 3.74	-1.26 ± 2.81
S_{LSR} (km s $^{-1}$)	279.23 ± 21.28	151.64 ± 15.26	225.79 ± 17.94
Galactic Orbit Parameters			
MW2014	T_p (Myr)	54 ± 8	37 ± 1
	Z_{max} (kpc)	0.507 ± 0.156	0.547 ± 0.010
	R_a (kpc)	2.100 ± 0.459	1.312 ± 0.196
	R_p (kpc)	0.199 ± 0.001	0.310 ± 0.131
	R_m (kpc)	1.149 ± 0.230	0.811 ± 0.163
	e	0.827 ± 0.041	0.618 ± 0.189
MW2014+Bar	Z_{max} (kpc)	0.510 ± 0.066	0.523 ± 0.021
	R_a (kpc)	2.843 ± 0.557	1.407 ± 0.021
	R_p (kpc)	0.220 ± 0.033	0.165 ± 0.155
	R_m (kpc)	1.531 ± 0.295	0.786 ± 0.088
	e	0.857 ± 0.050	0.790 ± 0.192
			0.352 ± 0.116

To refine these OCs' fundamental parameters and membership statistics, we utilise recent data from (Hunt & Reffert, 2024) in conjunction with our photometric analysis. While Hunt & Reffert (2024) reports 18, 55, and 776 members for HSC 25, HSC 37, and HSC 2878, respectively, our revised assessment identifies 44, 55, and 112 members. These discrepancies, particularly striking in the case of HSC 2878, likely stem from differences in membership selection criteria and the handling of background contamination.

The trigonometric parallaxes (ϖ) and corresponding parallax-based distances (d_{ϖ}) place the OCs at heliocentric distances between approximately 9.3 and 12.8 kpc. However, our isochrone fitting yields systematically smaller and more plausible distances: 7.36 ± 0.37 kpc for HSC 25, 6.79 ± 0.18 kpc for HSC 37, and 6.17 ± 0.22 kpc for HSC 2878. These values are consistent with the geometric distances (d_{BJ}) derived by Bailer-Jones et al. (2021) and the *dist50* estimates from Hunt & Reffert (2024). The large discrepancy between ϖ -based and isochrone-based distances likely stems from underestimated parallaxes in highly extinguished and crowded fields toward the Galactic centre, where Gaia's astrometric precision is significantly compromised.

The amount of extinction and reddening varies significantly among the three clusters. HSC 25 is the most heavily reddened, with a visual extinction of $A_V = 4.43$ mag and a colour excess of $E(B - V) = 1.41$ mag. HSC 37 exhibits a moderate extinction level ($A_V = 2.93$ mag, $E(B - V) = 0.94$ mag), while HSC 2878 is affected by the least amount of dust, with $A_V = 3.41$ mag and $E(B - V) = 1.09$ mag. These extinction patterns are consistent with the expected distribution of interstellar dust along lines of sight toward the inner Galaxy. Although substantial differential reddening is evident within each field, we corrected the extinction for each star individually based on its line-of-sight distance, minimising its impact on the distance and age determination.

Cluster mass estimates provide another layer of characterisation. In our analysis, HSC 25 and HSC 2878 display comparable total masses of 135 and 204 M_\odot , respectively, despite the larger number of members in HSC 2878. This indicates that HSC 2878 hosts a higher fraction of lower-mass stars, yielding a lower average stellar mass ($\langle M_C \rangle = 2.17 M_\odot$) compared to HSC 25 ($\langle M_C \rangle = 3.56 M_\odot$). In contrast, the markedly younger HSC 37 stands out with both the highest total mass (755 M_\odot) and the highest mean stellar mass (15.32 M_\odot), consistent with the presence of

massive, luminous stars characteristic of very young stellar populations.

The evolutionary state of each OC can also be assessed through its dynamical relaxation times. For HSC 25, the estimated relaxation time is 156 ± 54 Myr, compared to its age of 104 Myr, suggesting that it is still approaching full dynamical relaxation. HSC 2878, with a relaxation time of 214 ± 76 Myr and an age of about 1 Gyr, has likely experienced multiple relaxation cycles and can be considered dynamically evolved. In contrast, HSC 37, with a relaxation time of 31 ± 15 Myr but an age of only 4 Myr, remains in the very early stages of its dynamical evolution, likely retaining signatures of its initial conditions and being less influenced by long-term internal dynamical processes.

The LSR-corrected velocity components of HSC 25, HSC 37, and HSC 2878 indicate that, despite their common association with the Galactic bulge, they occupy different regions of velocity space, reflecting possible differences in their dynamical histories within the inner Galaxy. HSC 25 exhibits a high total velocity ($S_{\text{LSR}} = 279.23 \pm 21.28 \text{ km s}^{-1}$) dominated by a large negative V_{LSR} and a substantial vertical component ($W_{\text{LSR}} = 67.48 \pm 7.81 \text{ km s}^{-1}$), suggesting that it follows an orbit with significant excursions above and below the Galactic plane, possibly influenced by past dynamical heating or bar–bulge interactions. HSC 37 has the lowest total velocity of the sample ($S_{\text{LSR}} = 151.64 \pm 15.26 \text{ km s}^{-1}$), moderate radial motion, and a relatively small vertical velocity, indicating a more planar, less dynamically heated orbit that keeps it closely bound to the bulge region. HSC 2878, in contrast, is characterised by a large negative U_{LSR} ($-185.64 \pm 12.59 \text{ km s}^{-1}$), moderate tangential velocity, and negligible vertical motion, pointing to a highly eccentric, low-inclination orbit confined mainly to the bulge. These results show that bulge clusters can display a wide range of orbital shapes and inclinations, shaped by the complex dynamical environment of the inner Milky Way.

The kinematic properties of the open clusters (OCs), particularly their S_{LSR} values, 279.23 ± 21.28 , 151.64 ± 15.26 , and $225.79 \pm 17.94 \text{ km s}^{-1}$ for HSC 25, HSC 37, and HSC 2878, respectively, are considerably higher than the velocity dispersions typically observed among thin-disc stars. These high space motions suggest that the clusters may not be members of the canonical thin disc population, warranting further analysis of their orbits within both axisymmetric and barred Galactic potentials. Orbital integrations in the axisymmetric MW2014 model reveal that all three OCs remain relatively confined to the Galactic plane, with maximum vertical distances Z_{max} ranging from $0.396 \pm 0.015 \text{ kpc}$ (HSC 2878) to $0.547 \pm 0.010 \text{ kpc}$ (HSC 37). These vertical distances remain moderate even in the barred potential (MW2014+Bar), where Z_{max} values vary between $0.436 \pm 0.073 \text{ kpc}$ and $0.523 \pm 0.021 \text{ kpc}$.

Including the barred Galactic potential in the MW2014 potential model leads to noticeable variations in the derived orbital parameters for the analyzed clusters. In particular, the apocentric distance (R_a) shows the most pro-

nounced relative increase, reaching $\sim 35\%$ for HSC 25, $\sim 7\%$ for HSC 37, and $\sim 26\%$ for HSC 2878 compared to the axisymmetric case. Moderate changes are also observed in the mean orbital radius (R_m), with increases of $\sim 33\%$, -3% , and $\sim 7\%$ for the respective clusters. The eccentricities (e) exhibit enhancements of $\sim 4\%$, $\sim 28\%$, and more than twofold for HSC 2878, indicating that the bar component can significantly alter orbital shapes, particularly for low-eccentricity orbits. The vertical excursion (Z_{max}) remains relatively stable, with variations within a few percent, suggesting that the bar's influence is predominantly confined to the radial orbital structure rather than the vertical dynamics.

However, their radial orbital properties are notably distinct. HSC 25 exhibits a highly eccentric orbit, with $e = 0.827 \pm 0.041$ (MW2014) and $e = 0.857 \pm 0.050$ (MW2014+Bar), and plunges from a small pericentric distance ($R_p = 0.199 \pm 0.001 \text{ kpc}$) to a relatively extended apocentre ($R_a = 2.843 \pm 0.557 \text{ kpc}$). HSC 37 follows a similarly elliptical path with $e = 0.618 \pm 0.189$ in MW2014, increasing to $e = 0.790 \pm 0.192$ under the barred model. In contrast, HSC 2878 remains more tightly bound to the inner disc, showing the lowest eccentricities among the three ($e = 0.146 \pm 0.131$ in MW2014 and $e = 0.352 \pm 0.116$ in MW2014+Bar), and a narrower radial range. In terms of orbital time-scales, the clusters complete one revolution around the Galactic centre within approximately 54 ± 8 Myr for HSC 25, 37 ± 1 Myr for HSC 37, and 59 ± 1 Myr for HSC 2878, consistent with their varying orbital sizes and shapes.

Taken together, these results suggest that while all three clusters are moderately confined vertically, their planar orbital properties, particularly the high eccentricities and inner-Galaxy plunging orbits of HSC 25 and HSC 37, imply that they may have originated from, or interacted with, dynamically hotter Galactic components, or even formed in non-standard disc environments.

HSC 2878, on the other hand, shows signs of dynamical quiescence. Its low eccentricity and confinement to the Galactic plane, despite its advanced age, suggest it has avoided the kind of gravitational perturbations, such as interactions with molecular clouds or spiral arms, that typically increase orbital eccentricity over time (e.g., Wienlen, 1977; Quillen and Garnett, 2001; Aumer and Binney, 2009). The orbital and kinematic properties of HSC 25, HSC 37, and HSC 2878 indicate that, although all three are currently confined to the Galactic bulge, they have followed distinct dynamical paths. HSC 25 and HSC 2878 show signatures of dynamically heated or possibly accreted origins, whereas HSC 37 exhibits a cooler, more planar motion consistent with in-situ bulge formation.

These findings support the view that the three OCs do not share a common dynamical past and instead may represent a diverse population shaped by distinct formation environments and evolutionary processes. Future high-resolution spectroscopic studies of their chemical abundances, coupled with orbital integrations in time-

dependent, non-axisymmetric Galactic potentials, including bar and spiral arm perturbations, will be essential to constrain their origins and dynamical classifications further.

5. Acknowledgments

We would like to thank the anonymous referee for their helpful feedback and recommendations, which have contributed meaningfully to the improvement of our manuscript. This study presents results derived from the European Space Agency (ESA) space mission *Gaia*. The data from *Gaia* are processed by the *Gaia* Data Processing and Analysis Consortium (DPAC). Financial support for DPAC is provided by national institutions, primarily those participating in the *Gaia* Multi-Lateral Agreement (MLA). For additional information, the official *Gaia* mission website can be accessed at <https://www.cosmos.esa.int/gaia>, and the *Gaia* archive is available at <https://archives.esac.esa.int/gaia>. The authors would like to express their gratitude to the Deanship of Scientific Research at Northern Border University, Arar, KSA, for funding this research under project number "NBU-FFR-2026-237-04".

References

Aumer, M. and Binney, J.J., 2009, *Monthly Notices of the Royal Astronomical Society* **397**, 1286. doi:10.1111/j.1365-2966.2009.15053.x.

Alzhrani, A. Y., Haroon, A. A., Elsanhoury, W. H., & Çınar, D. C., 2025, *Journal of Astrophysics and Astronomy*, 46, 50. doi:10.1007/s12036-025-10076-6

Alzhrani, A. Y., Haroon, A. A., Elsanhoury, W. H., & Çınar, D. C., 2025, *Journal of Astrophysics and Astronomy*, 46, 58. doi:10.1007/s12036-025-10083-7

Banks T., Yontan T., Bilir S., Canbay R., 2020, JApA, 41, 6. doi:10.1007/s12036-020-9621-2

Bailer-Jones C. A. L., Rybizki J., Fouesneau M., Demleitner M., Andrae R., 2021, AJ, 161, 147. doi:10.3847/1538-3881/abd806

Bastian, N., Covey, K. R., & Meyer, M. R. 2010, *Annual Review of Astronomy and Astrophysics*, 48, 339. doi:10.1146/annurev-astro-082708-101642, arXiv:1001.2965

Binney, J. & Tremaine, S. 2008, *Galactic Dynamics*, 2nd ed., Princeton University Press

Bilir S., Güver T., Aslan M., 2006, AN, 327, 693. doi:10.1002/asna.200510614

Bilir, S., Ak, S., Karaali, S., Cabrera-Lavers, A., Chonis, T. S., Gaskell, C. M., 2008b, MNRAS, 384, 1178

Bilir S., Güver T., Khamitov I., Ak T., Ak S., Coşkunoğlu K. B., Paunzen E., et al., 2010, Ap&SS, 326, 139. doi:10.1007/s10509-009-0233-1

Bilir S., Bostancı Z. F., Yontan T., Güver T., Bakış V., Ak T., Ak S., et al., 2016, AdSpR, 58, 1900. doi:10.1016/j.asr.2016.06.039

Bisht, D., Zhu, Q., Yadav, R.K.S., Rangwal, G., Sariya, D.P., Durgapal, A., and, ...: 2022, *Publications of the Astronomical Society of the Pacific* **134**, 044201. doi:10.1088/1538-3873/ac6195.

Bisht, D., Zhu, Q., Elsanhoury, W.H., Yadav, R.K.S., Rangwal, G., Sariya, D.P., and, ...: 2022, *The Astronomical Journal* **164**, 171. doi:10.3847/1538-3881/ac8cf4.

Bisht, D., Jiang, I.-G., Elsanhoury, W.H., Belwal, K., Çınar, D.C., Raj A., Biswas S., et al., 2026, AJ, 171, 72. doi:10.3847/1538-3881/ae285b

Binney J., Gerhard O. E., Stark A. A., Bally J., Uchida K. I., 1991, MNRAS, 252, 210. doi:10.1093/mnras/252.2.210

Bobylev V. V., Bajkova A. T., 2017, ARep, 61, 551. doi:10.1134/S1063772917070010

Bostancı, Z. F., Ak, T., Yontan, T., Bilir, S., Güver, T., Ak, S., Çakırlı, Ö., Özdracan, O., Paunzen, E., De Cat, P., Fu, J. N., Zhang, Y., Hou, Y., Li, G., Wang, Y., Zhang, W., Shi, J., Wu, Y. 2015, MNRAS, 453, 1095–1107. doi:10.1093/mnras/stv1665, arXiv:1507.05968

Bostancı, Z. F., Yontan, T., Bilir, S., Ak, T., Güver, T., Ak, S., Paunzen, E., Başaran, Ç. S., Vurgun, E., Akti, B. A., Çelebi, M., Ürgüp, H. 2018, *Astrophys. Space Sci.*, 363, 143. doi:10.1007/s10509-018-3364-4, arXiv:1806.00947

Bovy, J., & Tremaine, S. 2012, ApJ, 756, 89. doi:10.1088/0004-637X/756/1/89

Bovy, J. 2015, ApJS, 216, 29. doi:10.1088/0067-0049/216/2/29

Bland-Hawthorn, J. and Gerhard, O.: 2016, *Annual Review of Astronomy and Astrophysics* **54**, 529. doi:10.1146/annurev-astro-081915-023441.

Bressan, A., Marigo, P., Girardi, L., Salasnich, B., Dal Cero, C., Rubele, S., & Nanni, A. 2012, MNRAS, 427, 127. doi:10.1111/j.1365-2966.2012.21948.x

Braga V. F., Contreras Ramos R., Minniti D., Ferreira Lopes C. E., Catelan M., Minniti J. H., Nikzat F., et al., 2019, A&A, 625, A151. doi:10.1051/0004-6361/201935103

Blitz L., Spergel D. N., 1991, *ApJ*, 379, 631. doi:10.1086/170535

Canbay R., Bilir S., Özdönmez A., Ak T., 2023, *AJ*, 165, 163. doi:10.3847/1538-3881/acbead

Canbay, R., Ak, T., Bilir, S., Soydugan, F., and Eker, Z.: 2025, *The Astronomical Journal* **169**, 87. doi:10.3847/1538-3881/ad9eb6.

Cantat-Gaudin, T., Anders, F., Castro-Ginard, A., et al. 2020, *A&A*, 640, A1. doi:10.1051/0004-6361/202038192

Cardelli J. A., Clayton G. C., Mathis J. S., 1989, *ApJ*, 345, 245. doi:10.1086/167900

Carrera, R., Casamiquela, L., Bragaglia, A., Carretta, E., Carbajo-Hijarrubia, J., Jordi, C., Alonso-Santiago, J., Balaguer-Nuñez, L., Baratella, M., D’Orazi, V., Lucatello, S., & Soubiran, C. 2022, *Astronomy and Astrophysics*, 663, A148. doi:10.1051/0004-6361/202243151, arXiv:2204.03765

Carvajal J. O., 2022, *VMSAI*, 2, 11. doi:10.36116/VIDEOMEM_2.2022.11

Chupina, N.V., Reva, V.G., and Vereshchagin, S.V.: 2001, *Astronomy and Astrophysics* **371**, 115. doi:10.1051/0004-6361:20010337.

Chupina, N.V., Reva, V.G., and Vereshchagin, S.V.: 2006, *Astronomy and Astrophysics* **451**, 909. doi:10.1051/0004-6361:20054009.

Çınar, D. C., Taşdemir, S., Koç, S., & Iyer, S. 2024, *Physics and Astronomy Reports*, 2, 1–17. doi:10.26650/PAR.2024.00002, arXiv:2404.13115

Çınar, D. C., Bilir S., Şahin T., Plevne O., 2025, *AJ*, 170, 13. doi:10.3847/1538-3881/add343

Çoşkunoğlu, B., Ak, S., Bilir, S., Karaali, S., Yaz, E., Gilmore, G., Seabroke, G. M., Bienaymé, O., Bland-Hawthorn, J., Campbell, R., Freeman, K. C., Gibson, B., Grebel, E. K., Munari, U., Navarro, J. F., Parker, Q. A., Siebert, A., Siviero, A., Steinmetz, M., Watson, F. G., & Wyse, R. F. G., Zwitter, T. 2011, *Monthly Notices of the Royal Astronomical Society*, 412(2), 1237–1245. doi:10.1111/j.1365-2966.2010.17983.x

Dwek E., Arendt R. G., Hauser M. G., Kelsall T., Lisse C. M., Moseley S. H., Silverberg R. F., et al., 1995, *ApJ*, 445, 716. doi:10.1086/175734

Eker, Z., Bilir, S., Yaz, E., Demircan, O., Helvacı, M., 2009, *AN*, 330, 68

Elsanhouri, W.H., Postnikova, E.S., Chupina, N.V., Vereshchagin, S.V., Sariya, D.P., Yadav, R.K.S., and ...: 2018, *Astrophysics and Space Science* **363**, 58. doi:10.1007/s10509-018-3268-3.

Elsanhouri, W. H., Haroon, A. A., Elkholly, E. A., & Çınar, D. C. 2025, *Journal of Astrophysics and Astronomy*, 46, 21. doi:10.1007/s12036-025-10044-0, arXiv:2412.07871

Feast M., Whitelock P., 1997, *MNRAS*, 291, 683. doi:10.1093/mnras/291.4.683

Gaia Collaboration, Brown, A. G. A., Vallenari, A., Prusti, T., de Bruijne, J. H. J., Babusiaux, C., Biermann, M., Creevey, O. L., Evans, D. W., Eyer, L., et al. 2021, *A&A*, 649, A1. doi:10.1051/0004-6361/202039657

Gaia Collaboration, Vallenari, A., Brown, A. G. A. ...: 2023, *Astronomy and Astrophysics*, 674, A1. doi:10.1051/0004-6361/202243940, arXiv:2208.00211.

Haroon, A. A., Ismaill, H. A., & Elsanhoury, W. H. 2017, *Astrophysics*, 60, 173.

Haroon, A. A., Elsanhoury, W. H., Elkholly, E. A., Saad, A. S., & Çınar, D. C. 2025, *Physica Scripta*, 100, 055006. doi:10.1088/1402-4896/abfb71

Hunt, E. L. & Reffert, S. 2024, *Astronomy and Astrophysics*, 686, A42. doi:10.1051/0004-6361/202348662, arXiv:2403.05143.

Jeffries, R. D., Thurston, M. R. & Hambly, N. C. 2001, 375, 863, doi:10.1051/0004-6361:20010918

Jurić, M., Ivezić, Ž., Brooks, A., Lupton, R. H., Schlegel, D., Finkbeiner, D., Padmanabhan, N.: 2008, *The Astrophysical Journal*, 673(2), 864. doi:10.1086/523619, arXiv:astro-ph/0510520.

King, I. 1962, *The Astronomical Journal*, 67, 471.

King, I. R. 1966, *The Astronomical Journal*, 71, 64.

Krone-Martins, A., & Moitinho, A. 2014, *A&A*, 561, A57. doi:10.1051/0004-6361/201321143

Kroupa, P. 2001, *Monthly Notices of the Royal Astronomical Society*, 322, 231. doi:10.1046/j.1365-8711.2001.04022.x

Lada, C. J. & Lada, E. A. 2003, *Annual Review of Astronomy and Astrophysics*, 41, 57. doi:10.1146/annurev.astro.41.011802.094844

Leggett, S.K.: 1992, *The Astrophysical Journal Supplement Series* **82**, 351. doi:10.1086/191720.

Liszt H. S., Burton W. B., 1980, *ApJ*, 236, 779. doi:10.1086/157803

Marshall, D. J., Robin, A. C., Reylé, C., Schultheis, M., Picaud, S., 2006, *A&A*, 453, 635

Molero M., Matteucci F., Spitoni E., Rojas-Arriagada A., Rich R. M., 2024, *A&A*, 687, A268. doi:10.1051/0004-6361/202450418

Nepal S., Chiappini C., Pérez-Villegas A., Queiroz A. B., Souza S., Steinmetz M., Anders F., et al., 2025, arXiv, arXiv:2507.06863. doi:10.48550/arXiv.2507.06863

Tanik Ozturk B., Bilir S., Yontan T., Plevne O., Ak T., Ak S., Canbay R., et al., 2025, AJ, 170, 164. doi:10.3847/1538-3881/adef0

Pecaut, M. J., & Mamajek, E. E. 2013, *The Astrophysical Journal Supplement Series*, 208(1), 9. doi:10.1088/0067-0049/208/1/9, arXiv:1307.2657

Perryman, M. A. C., Brown, A. G. A., Lebreton, Y., Gomez, A., Turon, C., Cayrel de Strobel, G., Mermilliod, J. C., Robichon, N., Kovalevsky, J., & Crifo, F. 1998, *Astronomy and Astrophysics*, 331, 81. doi:10.48550/arXiv.astro-ph/9707253, arXiv:astro-ph/9707253

Portail, M., Gerhard, O., Wegg, C., and Ness, M.: 2017, *Monthly Notices of the Royal Astronomical Society* **465**, 1621. doi:10.1093/mnras/stw2819.

Quillen, A.C. and Garnett, D.R.: 2001, *Galaxy Disks and Disk Galaxies* **230**, 87.

Riello, M., De Angeli, F., Evans, D. W., Montegriffo, P., Carrasco, J. M., Busso, G., Palaversa, L., et al. 2021, *A&A*, 649, A3. doi:10.1051/0004-6361/202039587

Sableviciute, I., Vansevicius, V., Kodaira, K., Narbutis, D., Stonkute, R., Bridzius, A.: 2006, *Baltic Astronomy*, 15, 547. doi:10.48550/arXiv.astro-ph/0701774, arXiv:astro-ph/0701774.

Salpeter, E. E. 1955, *The Astrophysical Journal*, 121, 161.

Sahin T., Bilir S., 2020, ApJ, 899, 41. doi:10.3847/1538-4357/aba2d2

Sales-Silva J. V., Cunha K., Smith V. V., Daflon S., Souto D., Guerço R., Queiroz A., et al., 2024, ApJ, 965, 119. doi:10.3847/1538-4357/ad28c2

Schlegel D. J., Finkbeiner D. P., Davis M., 1998, ApJ, 500, 525. doi:10.1086/305772

Schlafly E. F., Finkbeiner D. P., 2011, ApJ, 737, 103. doi:10.1088/0004-637X/737/2/103

Spitzer, J. L. & Hart, M. H. 1971, *The Astrophysical Journal*, 164, 399. doi:10.1086/150855.

Sun, M., Jiang, B., Yuan, H., & Li, J. 2021, *ApJS*, 254, 38. doi:10.3847/1538-4365/abf929

Taşdemir, S., & Çınar, D. C. 2025, *Contributions of the Astronomical Observatory Skalnaté Pleso*, arXiv:2501.17235. doi:10.48550/arXiv.2501.17235

Taşdemir, S., & Yontan, T. 2023, *Physics and Astronomy Reports*, 1, 1–10. doi:10.26650/PAR.2023.00001, arXiv:2304.14270

Taşdemir, S., Çınar, D. C., Canbay, R., Taştan, S., Eslanhoury, W., & Haroon, A. 2025, *Physics and Astronomy Reports*, 3, 1. doi:10.26650/PAR.2025.00003

Wielen, R.: 1977, *Astronomy and Astrophysics* **60**, 263.

Yontan, T., & Canbay, R. 2023, *Physics and Astronomy Reports*, 1, 65. doi:10.26650/PAR.2023.00008, arXiv:2310.13582

Yontan, T., Bilir, S., Bostancı, Z. F., Ak, T., Karaali, S., Güver, T., Ak, S., Duran, Ş., Paunzen, E. 2015, *Astrophys. Space Sci.*, 355, 267–281. doi:10.1007/s10509-014-2175-5, arXiv:1410.3129

Yontan, T., Çakmak, T., Bilir, S., et al. 2022, *RMxAA*, 58, 333–353. doi:10.22201/ia.01851101p.2022.58.02.14, arXiv:2207.06407

Yontan, T. 2023, *AJ*, 165, 79. doi:10.3847/1538-3881/aca6f0

Zoccali M., Valenti E., 2024, arXiv, arXiv:2412.01607. doi:10.48550/arXiv.2412.01607

Appendix A. List of Cluster Members

Table .6: Most probable members identified for HSC 25, HSC 37, and HSC 2878.

Order	Source ID	α (deg)	δ (deg)	G (mag)	R_{dist}	P
HSC 25						
1	4061893199113258752	265.4063	-25.7219	16.58	1.46	0.57
2	4061892511907882752	265.3709	-25.7297	16.18	2.02	0.53
3	4061894745291288064	265.4095	-25.6587	17.50	2.75	0.86
4	4061893714509852672	265.4497	-25.6971	17.62	3.15	0.63
5	4061941307090339584	265.3388	-25.6648	18.27	3.61	0.73
6	4061891554171656704	265.3665	-25.7647	19.24	4.02	0.51
7	4061892550662103680	265.3209	-25.7396	17.27	4.45	0.81
8	4067899526284562432	265.4623	-25.6431	18.70	5.19	0.71
9	4061941959956466176	265.3959	-25.6124	17.67	5.36	0.69
10	4061891962151801600	265.3212	-25.7718	17.90	5.68	0.63
11	4061891210573332736	265.3955	-25.7991	16.29	5.86	0.65
12	4061889934927280384	265.4769	-25.7645	15.23	5.96	0.65
13	4061942234803932160	265.3765	-25.5872	16.97	6.91	0.88
14	4061892099601587712	265.2803	-25.7648	18.18	7.11	0.72
15	4067947011429748864	265.3986	-25.5822	17.77	7.17	0.80
16	4061890278524824320	265.5349	-25.7388	16.33	8.06	0.57
17	4061946186175148032	265.3126	-25.5482	15.19	10.15	0.77
18	4067947385006693504	265.4735	-25.5340	16.60	10.99	0.54
19	4067948385819404928	265.4307	-25.5216	17.31	11.01	0.93
20	4061886675146119936	265.4450	-25.8816	16.22	11.18	0.80
21	4061943437425557888	265.1791	-25.6830	17.76	11.54	0.99
22	4067895815339514112	265.6164	-25.6471	16.88	12.59	0.97
23	4061884476059729536	265.2639	-25.8806	18.70	12.77	0.53
24	4061884269901201408	265.2710	-25.8873	19.05	12.91	0.85
25	4067900934943307904	265.5895	-25.5632	18.35	13.55	0.98
26	4061880352953047936	265.4239	-25.9399	16.04	14.41	0.87
27	4061932717185725696	265.1553	-25.8139	19.27	14.43	0.75
28	4061880765208864768	265.3067	-25.9670	18.29	16.57	0.93
29	4067896262013746944	265.7015	-25.6659	18.31	16.89	0.75
30	4067881040741568896	265.6795	-25.8308	18.02	17.38	0.71
31	4061938523962039296	265.0704	-25.6703	18.68	17.47	0.79
32	406193237358471936	265.0757	-25.7829	16.62	17.75	0.58
33	4061956837726296064	265.1023	-25.5602	16.98	17.80	0.93
34	406794996198029568	265.5405	-25.4280	16.58	18.29	0.50
35	406195962083595584	265.1901	-25.4511	19.33	18.57	0.77
36	4067897017928563584	265.7271	-25.6227	18.10	18.75	0.64
37	4061873137339617920	265.5121	-25.9988	18.78	18.99	0.67
38	4061957108227340416	265.0806	-25.5389	18.51	19.45	0.68
39	4061883131702799104	265.1403	-25.9446	16.89	19.92	0.54
40	4061890278524824320	265.5349	-25.7388	16.33	19.97	0.94
41	4061892511907882752	265.3709	-25.7297	16.18	19.97	0.87
42	4061892550662103680	265.3209	-25.7396	17.27	19.97	0.82
43	4061941959956466176	265.3959	-25.6124	17.67	19.97	0.82
44	4061942234803932160	265.3765	-25.5873	16.97	19.98	0.85
HSC 37						
1	4116297863470964864	264.3393	-24.3909	17.72	1.24	0.53
2	4116296725211705856	264.3593	-24.4365	16.02	1.86	0.63
3	4116297485513746304	264.3397	-24.3811	14.66	2.85	0.62
4	4116296523441351040	264.2847	-24.4011	16.51	3.85	0.75
5	4116292155366332928	264.3874	-24.4797	17.93	4.78	0.68
6	4116292125394285312	264.3724	-24.4983	15.53	5.64	0.56
7	4116297382340345472	264.4557	-24.3732	18.00	5.84	0.67
8	4116308201364443136	264.2470	-24.4073	17.56	5.90	0.59
9	4116293946460332928	264.4693	-24.4436	16.00	6.64	0.76
10	4116291575543116416	264.3296	-24.5359	18.71	7.94	0.97
11	4116292258445416576	264.4678	-24.5275	15.60	9.56	0.59
12	4116309373893519488	264.1895	-24.3517	19.82	9.61	0.88
13	4110291093956974080	264.1933	-24.4706	19.33	9.66	0.54
14	4116299336552012416	264.5403	-24.3934	17.34	10.15	0.73
15	4116299375202774656	264.5542	-24.3835	17.70	10.96	0.80
16	4116300612154452480	264.5483	-24.3477	17.53	11.12	0.99
17	4116291678717750016	264.3315	-24.5123	16.40	11.12	0.89
18	4116317719016015104	264.3607	-24.2156	18.70	11.41	0.93
19	4116292395884419840	264.4837	-24.5094	14.44	11.41	0.52
20	4116296415974109568	264.2700	-24.4237	16.93	11.95	0.63
21	4116296415974136960	264.2746	-24.4177	17.15	12.16	0.83
22	4116296690868885760	264.3881	-24.4368	17.78	12.31	0.84
23	4116296793931220608	264.3913	-24.4265	16.47	12.39	0.82
24	4116297343687195008	264.4347	-24.3902	18.72	12.81	0.76
25	4068251954064951168	264.4666	-24.5936	18.30	12.81	0.59
26	4116302501941006080	264.5595	-24.3010	18.87	12.82	0.96
27	4116302261519760512	264.5974	-24.3077	18.09	13.24	0.94
28	4068254187448027648	264.5726	-24.5030	18.51	13.24	0.53
29	4116302982976940800	264.6237	-24.2634	18.73	13.39	0.85
30	4116315210755065216	264.2465	-24.2055	18.26	13.39	0.52
31	4116297034449477632	264.3533	-24.4072	15.14	13.73	0.65

32	4068251473028317056	264.4500	-24.6184	18.80	13.78	0.78
33	4116305491238710656	264.5679	-24.2751	18.59	14.03	0.87
34	4068251438668414336	264.4451	-24.6283	18.28	14.23	0.71
35	4110285042307239296	264.2946	-24.6367	18.73	14.25	0.99
36	4116305074629133952	264.4995	-24.2516	17.81	14.25	0.97
37	4116318925900274304	264.4420	-24.1788	18.20	14.42	0.67
38	4116305933622762112	264.5406	-24.2268	17.73	14.77	0.88
39	4116305628677630720	264.5834	-24.2634	18.19	15.13	0.57
40	4116319922429152512	264.4501	-24.1404	18.06	15.40	0.74
41	4110285012282893696	264.2741	-24.6521	16.10	15.43	0.78
42	4116320678343548544	264.4470	-24.0812	17.80	15.43	0.62
43	4116303051832779008	264.5981	-24.2558	17.52	16.05	0.96
44	4116313359717558656	264.0819	-24.2898	20.32	16.47	0.71
45	4116302330140804096	264.6336	-24.2971	19.21	16.56	0.86
46	41102846684646272	264.3093	-24.6789	18.16	16.58	0.86
47	4116321807825166464	264.3377	-24.1210	18.43	17.11	0.67
48	4116307484200635136	264.5251	-24.1652	17.42	17.17	0.97
49	4116307587185626752	264.5395	-24.1630	17.86	17.72	0.96
50	4068249411508299008	264.5781	-24.6204	17.59	17.73	0.82
51	4116301677304415488	264.6741	-24.3132	18.41	18.30	0.92
52	4068259577590439936	264.6853	-24.4830	17.78	18.63	0.78
53	4110308239466721280	264.0139	-24.3644	17.72	18.80	0.59
54	4068249342720707840	264.6126	-24.6175	17.65	18.96	0.73
55	4116320403369755648	264.4661	-24.1064	19.28	18.96	0.85

HSC 2878						
1	5976514135629669760	256.1042	-37.0103	17.42	0.11	0.62
2	5976701671108223360	256.0770	-37.0171	16.65	1.25	0.50
3	5976513620263457280	256.0645	-37.0400	18.87	2.51	0.52
4	5976519805019042304	256.1616	-36.9960	17.90	2.99	0.50
5	5976707817166021760	256.1196	-36.9516	15.62	3.65	0.50
6	5976513001799309696	256.1650	-37.0485	17.91	3.78	0.78
7	5976702186504436224	256.0727	-36.9493	16.64	3.94	0.58
8	5976702908059382144	256.0535	-36.9491	18.33	4.36	0.76
9	5976702392618718848	256.0127	-36.9826	17.52	4.60	0.69
10	5976702942374695296	256.0625	-36.9390	18.78	4.70	0.58
11	5976512795601081216	256.1752	-37.0660	19.84	4.83	0.54
12	5976699712554813056	256.0037	-37.0663	18.12	5.77	0.50
13	5976518769884329600	256.2317	-37.0348	17.50	6.38	0.63
14	5976509771942057088	256.2019	-37.0840	18.27	6.50	0.54
15	5976699884353567232	255.9820	-37.0645	19.87	6.59	0.50
16	5976519457078122624	256.2427	-36.9865	17.82	6.90	0.68
17	5976519152183954432	256.2469	-37.0123	17.62	6.94	0.61
18	5976702491405715456	255.9596	-36.9821	16.26	7.03	0.63
19	5976519250920735360	256.2491	-36.9886	16.94	7.18	0.54
20	5976519186543228288	256.2619	-37.0034	16.29	7.68	0.63
21	5976512138454675840	256.1376	-37.1413	18.00	8.02	0.71
22	5976709436365594752	256.1020	-36.8742	18.47	8.19	0.50
23	5976512035377017728	256.1283	-37.1475	18.28	8.30	0.56
24	5976512001017260288	256.1100	-37.1559	18.38	8.72	0.50
25	5976509084777223936	256.1298	-37.1548	17.61	8.75	0.50
26	5976509084777212288	256.1381	-37.1544	19.40	8.79	0.69
27	5976709264613265408	256.0815	-36.8650	16.57	8.80	0.56
28	5976521145048449536	256.2559	-36.9297	17.41	8.84	0.70
29	5976510729705387904	256.0441	-37.1540	17.45	9.03	0.61
30	5976509325265076480	256.1905	-37.1438	20.35	9.04	0.50
31	5976705622477958400	255.9332	-36.9420	18.67	9.08	0.67
32	5976515303861745792	256.2437	-37.1118	20.36	9.10	0.54
33	5976706309629640576	256.0000	-36.8782	17.81	9.34	0.57
34	5976521935322475904	256.2499	-36.9085	19.82	9.38	0.50
35	5976509119101964032	256.1559	-37.1636	19.13	9.53	0.50
36	5976709638231918464	256.0851	-36.8505	16.79	9.65	0.66
37	5976511386845424896	255.9759	-37.1430	19.13	9.97	0.50
38	597651471977568000	256.2837	-37.0926	18.52	9.99	0.75
39	5976515888008710144	256.3058	-37.0501	17.08	10.05	0.57
40	5976511386845440128	255.9709	-37.1426	18.65	10.10	0.64
41	597669940332193216	255.9172	-37.0989	20.11	10.31	0.50
42	5976510493526489088	256.0907	-37.1842	14.28	10.42	0.56
43	5976511112001942784	256.0023	-37.1679	16.21	10.57	0.56
44	5976517812162823552	256.3195	-36.9759	19.10	10.63	0.88
45	5976508878588286080	256.1870	-37.1745	19.63	10.64	0.64
46	5976704145009189760	255.8789	-36.9926	16.69	10.74	0.50
47	5976508122704928256	256.1978	-37.1739	17.82	10.81	0.50
48	597671026099681472	256.1723	-36.8386	18.64	10.87	0.63
49	5976508771200255360	256.1417	-37.1904	16.82	10.94	0.53
50	5976511112001956480	255.9896	-37.1698	14.40	10.95	0.75
51	5976507538554018944	256.1027	-37.1961	19.36	11.12	0.72
52	5976712734946894976	256.0604	-36.8275	15.79	11.17	0.54
53	5976515162113372672	256.3256	-37.0650	19.38	11.20	0.85
54	5976522347608711040	256.2621	-36.8631	20.38	11.73	0.88
55	5976517532933798272	256.3462	-36.9963	17.70	11.73	0.63
56	5976706825025860224	255.9071	-36.8913	19.56	11.77	0.50
57	5976517949592644608	256.3404	-36.9515	17.44	11.97	0.73
58	5976700365390156672	255.8656	-37.0775	20.04	12.00	0.89
59	5976510218613863424	256.0218	-37.2016	19.86	12.08	0.50

60	5976705004002716416	255.8600	-36.9512	16.33	12.14	0.50
61	5976605154573384448	255.9148	-37.1478	20.17	12.16	0.50
62	5976605360731824256	255.9104	-37.1455	20.19	12.23	0.53
63	5976508221444115328	256.2312	-37.1865	18.95	12.23	0.61
64	5976522721256048768	256.2653	-36.8518	18.44	12.34	0.52
65	5976516884405080576	256.3596	-37.0067	19.15	12.35	0.71
66	5976516678282154624	256.3600	-37.0342	16.97	12.44	0.52
67	5976510111249265664	256.0149	-37.2062	17.97	12.45	0.62
68	5976509978130811392	256.0559	-37.2163	20.03	12.53	0.50
69	5976707026891755392	255.8992	-36.8772	16.55	12.60	0.94
70	5976711119990305664	256.1586	-36.7982	18.30	13.04	0.91
71	5976706928148136832	255.8743	-36.8914	18.58	13.05	0.50
72	5976518327514357376	256.3641	-36.9463	18.47	13.15	0.92
73	5976605326368710528	255.8863	-37.1554	20.46	13.48	0.65
74	5976606146700353536	255.8644	-37.1355	18.36	13.61	0.58
75	5976518464953395200	256.3700	-36.9236	18.90	13.87	0.50
76	5976506743979176064	256.0878	-37.2492	17.70	14.33	0.54
77	5976417103739787648	255.9489	-37.2167	18.58	14.37	0.50
78	5976718713491140992	255.8523	-36.8746	18.45	14.49	0.64
79	5976704832204061824	255.8013	-36.9644	17.29	14.67	0.50
80	5976606077980856576	255.8410	-37.1481	18.60	14.97	0.95
81	5976496165484562944	256.2922	-37.2207	20.14	15.55	0.59
82	5976502865631133568	256.3929	-37.1275	20.01	15.60	0.88
83	5976415969885811072	256.0156	-37.2653	17.99	15.82	0.91
84	5976495955019241600	256.2555	-37.2448	18.06	15.85	0.54
85	5976506091139537152	256.1802	-37.2678	19.02	15.87	0.62
86	5976610823980364160	255.7649	-37.0232	20.02	16.16	0.50
87	5976716720626283392	255.7674	-36.9412	17.47	16.57	0.62
88	5976610823930633344	255.7520	-37.0163	17.86	16.77	0.93
89	5976605940541912064	255.7923	-37.1418	18.15	16.78	0.62
90	5976501903560969344	256.3923	-37.1708	18.67	16.90	0.63
91	5976622678041516288	255.7483	-36.9906	20.40	16.99	0.94
92	5976605601246736896	255.8187	-37.1820	18.28	17.01	0.54
93	5976502006637520768	256.4324	-37.1373	19.42	17.55	0.50
94	5976716789397507968	255.7414	-36.9482	19.60	17.68	0.55
95	5976506503458792704	256.0688	-37.3058	17.95	17.78	0.94
96	5976725581144747392	255.9149	-36.7549	17.50	17.78	0.50
97	5976416755817554816	255.8898	-37.2564	18.45	17.89	0.84
98	5976542134506734848	256.4331	-36.8696	17.65	18.00	0.93
99	5976501285114858880	256.3659	-37.2273	15.72	18.12	0.65
100	5976541932695419264	256.4402	-36.8752	17.02	18.14	0.65
101	5976495650083822848	256.2674	-37.2845	18.84	18.23	0.50
102	5976541108031789824	256.4652	-36.9107	19.74	18.42	0.89
103	5976734312868607232	256.2993	-36.7472	16.39	18.43	0.92
104	5976416450906116096	255.8968	-37.2754	20.27	18.67	0.92
105	5976623021637925120	255.7171	-36.9524	18.75	18.78	0.53
106	5976725752947556736	255.9533	-36.7198	18.37	18.86	0.84
107	5976501044596678144	256.3805	-37.2368	17.74	19.02	0.51
108	5976715032711487104	256.1908	-36.7013	18.48	19.05	0.86
109	5976542581183416960	256.4309	-36.8329	15.18	19.05	0.87
110	5976715032711489408	256.1951	-36.7009	19.45	19.12	0.50
111	5976717820142606208	255.7316	-36.8909	18.48	19.16	0.81
112	5976726581926205312	255.9259	-36.7103	19.56	19.91	0.91